

# Dynamic simulations of shear-flow-induced chirality and twisted-texture transitions of a liquid-crystalline polymer

W. H. Han and A. D. Rey\*

*Department of Chemical Engineering, McGill University, 3480 University Street, Montreal, Quebec, Canada H3A 2A7*

(Received 22 July 1993)

An alternative computational adaptive method to solve the Leslie-Ericksen equations of nematic hydrodynamics is presented. The method uses adaptive torque balances and is able to accurately compute arbitrary three-dimensional orientation fields. The method is applied, in conjunction with computational bifurcation methods, to solve the governing equations for a model rigid-rod, non-aligning, nematic polymer, in steady and transient rectilinear simple shear flows, using fixed parallel director anchoring. The five-component solution vector consists of the primary and secondary velocity components and the three-dimensional director field  $\mathbf{n}$ . The parameter space is the line representing the magnitudes of the Ericksen number ( $\mathcal{E}$ ). According to the magnitude of  $\mathcal{E}$ , seven types of stable steady-state solutions are found and fully characterized. The seven types of solutions are classified as in-plane solutions if the director remains within the shear plane, defined by the flow direction and the velocity gradient, and as out-of-plane (OP) solutions if the director field is out of the shear plane (three-dimensional orientation). The six OP solutions are three pairs of mirror-image solutions that differ from each other by their rotation number ( $\Lambda$ ). Two pairs of out-of-plane solution branches are achiral ( $\Lambda = 0$ ) and display one-way twisting from the shear plane. One pair of out-of-shear-plane solution branches is chiral ( $\Lambda = \pm 1$ ) and displays a full  $2\pi$  director rotation when going from the bottom plate to the top plate. The nucleation mechanisms of these chiral branches are identified using a torque analysis. The main bifurcation phenomena and the local stability of the branches are summarized in a bifurcation diagram. The main structural changes, as the parameter  $\mathcal{E}$  increases, are captured by visualization of the transient director field. The main features of the velocity field are captured by particle tracking visualization, which yields three-dimensional particle motions driven by the combined primary and secondary flows. The main mechanical responses, captured by the transient rheological functions (apparent viscosity and the first normal stress differences) exhibit, at low shear rates, non-Newtonian responses that are usually found in isotropic, viscous, or viscoelastic liquids, at large shear rates. Dynamic simulation in conjunction with the bifurcation diagram is used to construct the stability phase diagram, which yields the adopted stable steady-state solution that results from shearing a monodomain sample with fixed parallel director anchoring. Finally, the strain history is shown to control the finally adopted steady state, thus invalidating linear superposition which is usually valid at small shear rates.

PACS number(s): 64.70.Md, 47.20.Ft, 02.70.-c, 47.50.+d

## I. INTRODUCTION

The macroscopic description of dynamical phenomena of nematic liquid crystals requires the specification of the velocity field  $\mathbf{v}(\mathbf{x},t)$ , the pressure field  $p(\mathbf{x},t)$ , and, at least, the tensor order parameter field  $\mathbf{Q}(\mathbf{x},t)$ , which is a symmetric traceless second order tensor [1]. In some cases, the eigenvalues of  $\mathbf{Q}$  can be taken to be constant and the dynamics of the microstructure of the orientationally ordered viscoelastic rigid rod nematics may be captured by variations in a single eigenvector of  $\mathbf{Q}$ , usually called the director  $\mathbf{n}(\mathbf{x},t)$ . A situation of practical interest, in which the assumption is valid, is the simple shear creeping flow of rigid rod, uniaxial, thermotropic (lyotropic) nematic polymers at temperatures (concentrations) corresponding to their full nematic state, which is captured by the director theory of Leslie and Ericksen (LE) [2]. A distinguishing feature of rigid rodlike nematic

polymers, as compared to low molar mass nematics, is the strong anisotropy in their viscoelastic constants, usually characterized by the three elastic constants of splay ( $K_{11}$ ), twist ( $K_{22}$ ), and bend ( $K_{33}$ ), and the six Leslie coefficients  $\{\alpha_i\}$ ,  $i=1,2,\dots,6$ . These anisotropies are known [3] to cause a wide variety of pattern-formation phenomena in field-induced transitions. Field-induced pattern-formation phenomena in nematic polymer systems include periodic banding and stripe formations [4–8]; agreements between the LE theoretical predictions and experimental results have been reported for pattern formations in the presence of magnetic fields [8,9] and shear flows [10]. In this paper we present the results of a numerical study, using the full LE theory, of shear-flow-induced transitions in nematic polymers, which also predict a rich variety of pattern formation phenomena.

A fundamental rheological property of nematics is whether or not they align in the direction of flow during a shearing motion. The LE theory is able to describe both types of behavior. For low molar mass nematics, a transition from aligning to nonaligning modes is usually experimentally observed whenever a thermotropic nematic is brought to a temperature approaching that

\*Electronic address: inaf@musicb.mcgill.ca

of the nematic-smectic transition [11,12]. On the other hand, it is generally agreed that many nematic polymers do not flow align in shear [13]. The single parameter that controls the orienting behavior during shear flow is the tumbling or reactive parameter  $\lambda$  [2]. A classification of shear-flow-orienting behavior for low molar mass uniaxial liquid crystal has been given by Carlsson [14]. Briefly, for rigid-rod-like nematics, if  $\lambda > 1$ , the director aligns close to the shear-flow direction, while for discotic nematics, if  $\lambda < -1$ , the director aligns close to the normal to the shear-flow direction, in both cases within the shear plane defined by the flow direction and the velocity gradient. On the other hand, if  $0 < \lambda < 1$  ( $-1 < \lambda < 1$ ), rodlike (discotic) nematics do not flow align in shear, meaning that there is no particular orientation at which the viscous torque arising from the combined effects of vorticity and strain cancel each other. The corresponding classification of flow orienting behavior for nematic polymeric liquids has been given by Farhodi and Rey [15]. Briefly, if the effect of flow on the scalar order parameter  $S$  is taken into account, the tumbling parameter  $\lambda$  for low molar mass uniaxial nematic liquid crystals becomes the tumbling function  $\lambda(S)$  for uniaxial nematic polymers. The rheological behavior is now sensitive to the shear rate magnitude, and a rich variety of nonlinear dynamical features arises from the possible shear-induced aligning-nonaligning transitions. Experimental data seem to indicate [16–18] that for sufficiently small shear rates, the assumption that  $\lambda$  is a constant and less than one should be adequate to describe the slow dynamical behavior of nonaligning, rigid-rod, uniaxial nematic polymers.

The details of the orienting behavior of nematic polymers at low shear rates are at present not clearly understood, although the following rheo-optical experiments indicate the following: (i) During shear start-up flows of PBT (poly 1,4-phenylene-2, 6-benzobisthiazole) [19] with controlled surface orientation and of PBG (poly-benzyl-glutamate) without controlled surface orientation [20], there are long-lasting light transmission fluctuations whose exact origin is not yet known. (ii) Conoscopic studies of shear start-up flows of monodomain PBT, using controlled surface orientation, show that initially the angle between optic axis (director) and the flow director is negative, and that for sufficiently large strains the director escapes the plane of shear [19,21]. For some conditions it is reported that director fields displays twisted out-of-plane surface layers with an almost in-plane orientation at the midgap region [19]. (iii) Conoscopic studies of aligned and nonaligned melts of a main chain thermotropic nematic polyester, subjected to shearing flow, show that the director is of the aligning type close to the nematic-isotropic transition temperature and of the non-aligning type close to the smectic-nematic phase transition [22]. (iv) Two types of shear-induced pattern formations, band or stripe, were experimentally observed without controlled surface orientations and were characterized as a function of initial orientation and the Deborah and Ericksen numbers [6,7].

The main results of previous numerical studies of various shear flows of nonaligning nematics, using the LE equations of nematodynamics, that have explored the in-

plane (IP) to out-of-plane (OP) flow-induced orientation instabilities and transitions are as follows: (i) Zuniga and Leslie [23] show, using the parameter values of 8CBP (4-n-octyl-4'-cyanobiphenyl), parallel and homeotropic fixed director wall anchorings, spatially one-dimensional solutions, and linear stability analysis, that the LE equations predict that the two-dimensional in-plane orientation becomes unstable to three-dimensional infinitesimal perturbations, at a critical value of the Ericksen number  $\mathcal{E}_{co}$ , which is generally lower than the one corresponding to in-plane tumbling instability  $\mathcal{E}_{ci}$ , in agreement with the experiments [24]. The only exception to the ordering  $\mathcal{E}_{co} < \mathcal{E}_{ci}$  occurs when using a particular set of material parameters and homeotropic anchoring, in which case  $\mathcal{E}_{co}$  is slightly greater than  $\mathcal{E}_{ci}$ , but nevertheless this case eventually leads to further instabilities. (ii) The same critical Ericksen number ordering ( $\mathcal{E}_{co} < \mathcal{E}_{ci}$ ) results were obtained for the Taylor-Couette flow of 8CBP with homeotropic wall anchoring [25]. The only exception for the Taylor-Couette flow is that there is some small interval of  $\mathcal{E}$  values for which there is a stable IP solution branch even if  $\mathcal{E} < \mathcal{E}_{co}$ . (iii) Luskin and Pan [26] show, using the parameter values of 8CBP and parallel fixed director wall anchoring, that the LE equations predict steady out-of-plane solutions, whenever  $\mathcal{E} > \mathcal{E}_{co}$ ; cases for which  $\mathcal{E}_{ci} < \mathcal{E}_{co}$  were obtained for certain parameter values. (iv) Han and Rey used numerical bifurcation methods and the same material constants as Zuniga and Leslie [23] and confirmed that  $\mathcal{E}_{co} < \mathcal{E}_{ci}$  for all the parameter sets and director anchoring conditions. They found that there are stable steady state out-of-plane orientation solution branches, that bifurcate supercritically, from the in-plane solution branch [27]. Their transient simulation results show long lasting director fluctuations and underdamped oscillations of the rheological functions [28]. For a nematic polymer, they showed that the IP-OP orientational transition can be either supercritical, subcritical, or tricritical, depending on the surface orientation and on the anisotropy of the Frank elastic constants [29]. A detailed comparison between these numerical simulations is available in [28].

The objectives of this paper are (i) to present a numerical scheme that allows for the solution of LE equations of nematodynamics for arbitrary director fields, (ii) to present results of a numerical study of the rectilinear creeping shear flow of a nonaligning nematic polymer for values of the Ericksen number considerably higher than those associated with the IP-OP orientational transition previously considered, and (iii) to characterize and visualize the associated nonlinear flow phenomena such as bifurcations, multistability, secondary flows, and history dependence.

The organization of this paper is as follows. Section II presents the governing equations, numerical methods, and input data. Section III presents the bifurcation diagram, the orientational instabilities, the characteristic velocity and director fields, particle tracking and director dynamic visualizations, the phase stability diagram, a study of relaxation and flow reversal phenomena, and a characterization of the history dependence of the adopted stable steady states. Finally, conclusions are given.

## II. THEORY AND NUMERICAL METHODS

### A. The Leslie-Ericksen equations

The Leslie-Ericksen theory consists of the linear momentum balance, director torque balance, and constitutive equations for the stresses, viscous, and elastic torques [2]. The linear momentum balance is

$$\rho \dot{\mathbf{v}} = \mathbf{f} + \nabla \cdot \boldsymbol{\sigma}, \quad (1)$$

where  $\rho$ ,  $\mathbf{v}$ ,  $\mathbf{f}$ , and  $\boldsymbol{\sigma}$  are the density, velocity, body force per unit volume, and total stress, respectively. The superposed dot signifies the material time derivative. The constitutive equation for the total stress tensor  $\boldsymbol{\sigma}$  is

$$\boldsymbol{\sigma} = -p\boldsymbol{\delta} - \frac{\partial F}{(\partial \nabla \mathbf{n})^T} \cdot \nabla \mathbf{n} + \alpha_1(\mathbf{nn} : \mathbf{A})\mathbf{nn} + \alpha_2 \mathbf{nN} + \alpha_3 \mathbf{Nn} + \alpha_4 \mathbf{A} + \alpha_5 \mathbf{nn} \cdot \mathbf{A} + \alpha_6 \mathbf{A} \cdot \mathbf{nn}, \quad (2)$$

where  $p$ ,  $\boldsymbol{\delta}$ ,  $\alpha_i$  ( $i = 1, \dots, 6$ ),  $\mathbf{A}$ , and  $\mathbf{N}$  are the pressure, unit tensor, Leslie viscosity coefficients, rate of deformation tensor, and corrotational time derivative of  $\mathbf{n}$ , respectively. The last two quantities are given by

$$2\mathbf{A} = [\nabla \mathbf{v} + (\nabla \mathbf{v})^T], \quad (3)$$

$$\mathbf{N} = \dot{\mathbf{n}} - \boldsymbol{\omega} \cdot \mathbf{n}, \quad (4)$$

where the rate of rotation tensor  $\boldsymbol{\omega}$  is

$$2\boldsymbol{\omega} = [\nabla \mathbf{v} - (\nabla \mathbf{v})^T]. \quad (5)$$

The Frank orientation curvature elastic energy  $F$  is given by

$$2F = K_{11}(\nabla \cdot \mathbf{n})^2 + K_{22}(\mathbf{n} \cdot \nabla \times \mathbf{n})^2 + K_{33} |\mathbf{n} \times \nabla \times \mathbf{n}|^2, \quad (6)$$

where  $K_{11}$ ,  $K_{22}$ , and  $K_{33}$  are the splay, twist, and bend constants, respectively. The director torque balance is given by

$$\mathbf{0} = \boldsymbol{\Gamma}^v + \boldsymbol{\Gamma}^e. \quad (7)$$

The unit length director condition is

$$1 = \mathbf{n} \cdot \mathbf{n}. \quad (8)$$

The viscous torque  $\boldsymbol{\Gamma}^v$  and the elastic torque  $\boldsymbol{\Gamma}^e$ , in the fixed Cartesian coordinate system  $(x, y, z)$ , are given by

$$\boldsymbol{\Gamma}^v = -\mathbf{n} \times (\gamma_1 \mathbf{N} + \gamma_2 \mathbf{A} \cdot \mathbf{n}), \quad (9)$$

$$\boldsymbol{\Gamma}^e = -\mathbf{n} \times \left( \frac{\partial F}{\partial \mathbf{n}} - \nabla \cdot \frac{\partial F}{\partial (\nabla \mathbf{n})^T} \right), \quad (10)$$

where  $\gamma_1$  and  $\gamma_2$  are the rotational and irrotational viscosities given by

$$\gamma_1 = \alpha_3 - \alpha_2, \quad (11)$$

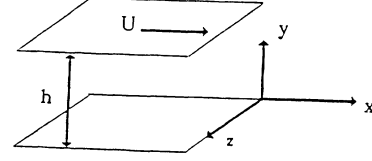


FIG. 1. Schematic of simple shear flow and definition of fixed coordinate system  $(x, y, z)$ .

$$\gamma_2 = \alpha_6 - \alpha_5. \quad (12)$$

Figure 1 shows the flow geometry. A typical non-aligning nematic polymer (PBG) is placed between two parallel plates separated by a distance  $h$ . The upper plate is moving toward the positive  $x$  axis parallel to the primary velocity  $v_x$  with a speed  $U$ . The  $y$  axis is normal to the plate surface and the  $z$  axis is parallel to the secondary velocity  $v_z$ . The  $x$ - $y$  shear plane is defined by the velocity gradient direction ( $y$ ) and the flow direction ( $x$ ). Whenever  $n_z = 0$  the orientation is denoted as IP (in-shear plane), and whenever  $n_z \neq 0$  it is denoted as OP (out-of-shear plane).

### B. Adaptive torque balances

In this paper we present results using adaptive torque balances, similar to our previously formulated gyroscopic torque balance [29]. The adaptive orthogonal triad  $(\mathbf{n}, \mathbf{g}_1, \mathbf{g}_2)$  is defined by the director  $\mathbf{n}$  and the two gyrotors  $\mathbf{g}_1$  and  $\mathbf{g}_2$ ; the relationships between  $\mathbf{n}$ ,  $\mathbf{g}_1$ , and  $\mathbf{g}_2$  with respect to the fixed Cartesian coordinate system  $(x, y, z)$  are shown in Fig. 2. The torque balances have their axes of rotations collinear with the gyrotors  $\mathbf{g}_1$  and  $\mathbf{g}_2$ . The gyrotors and the director define an unknown rotating orthogonal coordinate system that satisfy the following two equations:

$$\mathbf{g}_2 = \frac{\mathbf{n} \times \mathbf{g}_1^*}{\|\mathbf{n} \times \mathbf{g}_1^*\|}, \quad \mathbf{g}_1 = \mathbf{g}_2 \times \mathbf{n}, \quad (13)$$

where  $\mathbf{g}_1^*$  denotes the known value of  $\mathbf{g}_1$  at the previously

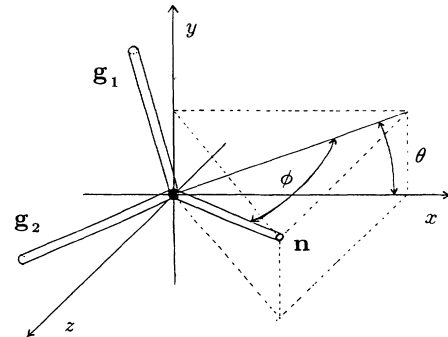


FIG. 2. Relationships between the two rectangular coordinate systems of  $(\mathbf{n}, \mathbf{g}_1, \mathbf{g}_2)$  and  $(x, y, z)$  and the spherical coordinate system  $(r=1, \phi, \theta)$ ;  $\phi$  is the twist angle and  $\theta$  is the tilt angle.

converged computation step. The transformation tensor  $\mathbf{T}$ , which maps  $(x, y, z)$  into  $(\mathbf{n}, \mathbf{g}_1, \mathbf{g}_2)$ , is given by

$$\mathbf{T} = \begin{pmatrix} \mathbf{n} \cdot \mathbf{i}_1 & \mathbf{n} \cdot \mathbf{i}_2 & \mathbf{n} \cdot \mathbf{i}_3 \\ \mathbf{g}_1 \cdot \mathbf{i}_1 & \mathbf{g}_1 \cdot \mathbf{i}_2 & \mathbf{g}_1 \cdot \mathbf{i}_3 \\ \mathbf{g}_2 \cdot \mathbf{i}_1 & \mathbf{g}_2 \cdot \mathbf{i}_2 & \mathbf{g}_2 \cdot \mathbf{i}_3 \end{pmatrix}, \quad (14)$$

where  $\mathbf{i}_1 = (1, 0, 0)$ ,  $\mathbf{i}_2 = (0, 1, 0)$ , and  $\mathbf{i}_3 = (0, 0, 1)$ . The fixed torque set  $(\mathbf{\Gamma}^v, \mathbf{\Gamma}^e)$ , given by Eqs. (9) and (10), is transformed into the adaptive torque set  $(\mathbf{\Gamma}^{v*}, \mathbf{\Gamma}^{e*})$  as follows:

$$\mathbf{\Gamma}^{v*} = -(\mathbf{T} \cdot \mathbf{n}) \times [\mathbf{T} \cdot (\gamma_1 \mathbf{N} + \gamma_2 \mathbf{A} \cdot \mathbf{n})], \quad (15)$$

$$\mathbf{\Gamma}^{e*} = -(\mathbf{T} \cdot \mathbf{n}) \times \left\{ \mathbf{T} \cdot \left[ \frac{\partial F}{\partial \mathbf{n}} - \nabla \cdot \left( \frac{\partial F}{\partial (\nabla \mathbf{n})^T} \right) \right] \right\}. \quad (16)$$

Then the corresponding adaptive torque balance equation becomes

$$\mathbf{0} = \mathbf{\Gamma}^{v*} + \mathbf{\Gamma}^{e*}. \quad (17)$$

The full equations are listed in the Appendix.

The principal feature of this formulation is the automatic selection of the two adaptive orthogonal gyrtors  $(\mathbf{g}_1, \mathbf{g}_2)$  as the torque axes; since the director is always orthogonal to  $(\mathbf{g}_1, \mathbf{g}_2)$ , the two necessary and sufficient torque balance equations are always linearly independent. The orthogonal adaptive triad is space and time dependent since it satisfies Eq. (17) and the mutual orthogonality between  $\mathbf{g}_1(y, t)$ ,  $\mathbf{g}_2(y, t)$ , and  $\mathbf{n}(y, t)$ . This spatiotemporal adaptation is smooth and continuous, as shown in Fig. 3 for a typical simulation [ $\mathcal{E}=466.9$ ,  $\mathbf{n}_{\text{wall}}=(1,0,0)$ ]; the corresponding shear strains ( $\gamma = Ut/h$ ) are  $A=0.0$ ,  $B=78.36$ ,  $C=87.34$ , and  $D=252.9$

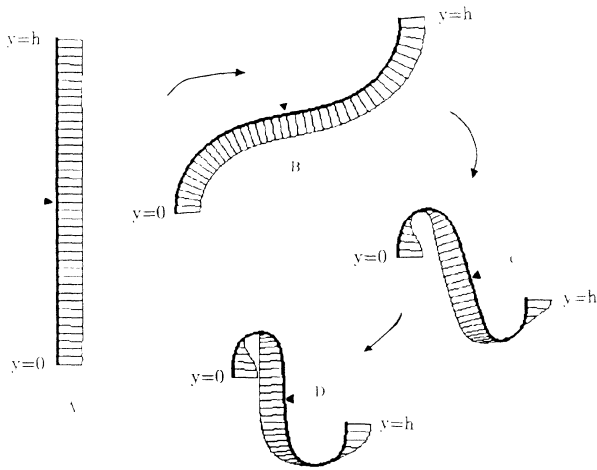


FIG. 3. Evolution of the adaptive torque triad  $(\mathbf{n}, \mathbf{g}_1, \mathbf{g}_2)$  for simple shear start-up flow ( $\mathcal{E}=466.9$ ), shown as deforming ribbons. The thick backbone line is tangential to  $\mathbf{g}_1$  and the thin side lines denote  $\mathbf{n}$ . The filled triangles indicate the centerline position on the deforming ribbon. The corresponding strains  $\gamma$  for each column are  $A=0.0$ ,  $B=78.36$ ,  $C=87.34$ , and  $D=252.9$  (steady state).

(steady state)]. The space curves traced by the tips of the director and by the tangent (thick backbone line) to  $\mathbf{g}_1$  define a ribbon, whose contour length is equal to the gap thickness; the thin line segments normal to the thick backbone line denote the director. The figure shows how the initial (A) orthogonal torque triad continuously deforms as the steady state (D) is reached; at each strain the filled triangle at the centerline ( $y = h/2$ ) serves to indicate the  $y$  coordinate on the spatially deforming ribbon.

Figure 4 shows a representative visualization of the director dynamics  $\mathbf{n}(y, t)$  across the thickness direction ( $y$ ) for  $\mathcal{E}=466.9$ , using the fixed torque balance equation (7); each column corresponds to the following strains:  $A=54.68$ ,  $B=76.16$ ,  $C=78.34$ ,  $D=79.94$ ,  $E=81.51$ , and  $F=89.15$ . The figure shows that the initially homogeneous director field (column A) evolves into a profile containing boundary singularities (column F) that eventually lead to computation breakdown. The cause of the breakdown is identified in column C, which shows that at this strain ( $\gamma = 78.34$ ), the director is oriented along the flow direction ( $x$ ) close to the bounding surface, but is aligned along the velocity gradient ( $y$ ) in the centerline region. The major advantage of using the adaptive method over a fixed torque balance methods are (i) improved accuracy due to the exact orthogonality between  $\mathbf{n}$ ,  $\mathbf{g}_1$ , and  $\mathbf{g}_2$ , and (ii) robust computational stability also due to the exact orthogonality. In addition to these advantages it turns out that for some complex orientation dynamics a fixed torque triad may break down due to numerical ill conditioning or linear dependence of the equations.

The Ericksen number  $\mathcal{E}$  defines the parameter space studied in this paper and is given by

$$\mathcal{E} = \frac{(\alpha_3 - \alpha_2)hU}{(K_{11}K_{22}K_{33})^{1/3}}. \quad (18)$$

The Reynolds number  $Re$  is defined as

$$Re = \frac{\rho U h}{\alpha_4} = \mathcal{E} \frac{\rho (K_{11}K_{22}K_{33})^{1/3}}{(\alpha_3 - \alpha_2)\alpha_4}. \quad (19)$$

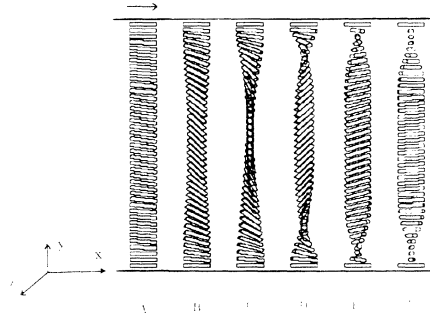


FIG. 4. Three-dimensional visualization of the director evolution leading to computational breakdown (fixed torque formulation). This figure shows the result of linear dependence or ill conditioning of the governing equations when using fixed torque balances: Column F shows a pair of surface singularities. Each column represents the following strains  $\gamma$ :  $A=54.68$ ,  $B=76.16$ ,  $C=78.34$ ,  $D=79.94$ ,  $E=81.51$ ,  $F=89.15$ , and the Ericksen number is  $\mathcal{E}=466.9$ .

where  $\alpha_4$  was used as a characteristic viscosity. A typical Reynolds number for the presented simulations is  $5 \times 10^{-7}$  ( $\mathcal{E}=300$ ). All transient results are shown as a function of the nominal strain  $\gamma$ , defined by

$$\gamma = \dot{\gamma}_n t, \quad (20)$$

where  $\dot{\gamma}_n = U/h$  is the nominal shear rate and  $U$  is the upper plate velocity. We note that the actual shear rate  $[\dot{\gamma}(y,t,\mathcal{E})]$  is not taken to be a given constant but is a computed function of time and space. Typical nominal shear rates for the simulations are of the order of  $10^{-3} \text{ sec}^{-1}$ . For the values used here the relation between the nominal shear strain rate  $\dot{\gamma}_n$  and the Ericksen number is  $\dot{\gamma}_n = 1.055 \times 10^{-5} \mathcal{E}$ .

The initial condition used throughout this paper are (i)  $\mathbf{v}(0,y)=0$ ,  $y \in [0,h]$  (no slip at the walls) and (ii)  $\mathbf{n}(0,y)=(1 + \epsilon_x, \epsilon_y, \epsilon_z)[(1 + \epsilon_x)^2 + \epsilon_y^2 + \epsilon_z^2]^{-\frac{1}{2}}$ ,  $y \in [0,h]$  (monodomain, randomly perturbed, alignment), where the magnitude of the random perturbations are restricted to  $\|\epsilon_x\|_1 = \|\epsilon_y\|_1 = \|\epsilon_z\|_1 = 10^{-2}$ . The boundary conditions are (i)  $\mathbf{v}(t,0)=\mathbf{v}(t,h)=0$ ,  $t \in \mathbb{R}^+$  (no flow) and (ii)  $\mathbf{n}(t,0)=\mathbf{n}(t,h)=\mathbf{n}_w=(1,0,0)$ ,  $t \in \mathbb{R}^+$  (fixed parallel anchoring).

The set of experimentally measured material constants for PBG [8], used in this paper, is shown in Table I. The gap width  $h$  is  $3.5 \times 10^{-4} \text{ m}$ , and the density  $\rho$  used in the dynamic simulation is  $10^3 \text{ kg/m}^3$ .

The model output is the solution vector that, for the dynamic simulations, consists of the velocity field  $\mathbf{v}(y,t) = (v_x(y,t), 0, v_z(y,t))$  and the director field  $\mathbf{n}(y,t) = (n_x(y,t), n_y(y,t), n_z(y,t))$ , and for the steady states  $\mathbf{v}(y) = (v_x(y), 0, v_z(y))$  and  $\mathbf{n}(y) = (n_x(y), n_y(y), n_z(y))$ .

In this work, the Galerkin finite-element method [30] with second order fully implicit time marching scheme, standard computational bifurcation methods [31], and the Newton-Raphson iteration method were used to construct the bifurcation diagrams and transient calculations. We used 200 linear elements, enforce the same accuracy on the numerical results, and employ the same convergence criteria as in [28]. All the equation manipulations used to obtain component equations, their Galerkin form, and Jacobians, are carried out using MATHEMATICA [32].

TABLE I. The Leslie viscosity coefficients and the Frank elastic constants for poly- $\gamma$ -benzyl-glutamate [7].

$\lambda$	0.9948
$\alpha_1$ (Pa s)	-3.66
$\alpha_2$	-6.92
$\alpha_3$	0.018
$\alpha_4$	0.348
$\alpha_5$	6.61
$\alpha_6$	-0.292
$K_{11}$ ( $10^{-11} \text{ N}$ )	1.21
$K_{22}$	0.078
$K_{33}$	0.763

### III. RESULTS AND DISCUSSION

#### A. Bifurcation analysis

Table II presents a definition of the terminology, symbols, and the main characteristics of the seven stationary solution branches discussed in the rest of this paper. The seven solution branches are classified according to their orientation dimensions, their chirality, the rotation number  $\Lambda$  or number of turns the director performs while going from the bottom plate to top plate, their orientation with respect to the shear plane, the maximum twist angle  $\phi$ , and the symmetry of the secondary velocity field  $v_z(y)$ . The four achiral out-of-plane OPN $\pm$  and OPS $\pm$  solutions may have one way left (-) or right (+) twist, where  $N$  means that the maximum out-of-plane angle  $|\phi|_{\text{max}}$  is always less than  $\pi/2$  radians and  $S$  means that  $|\phi|_{\text{max}}$  is always less than  $\pi$  radians. The two chiral out-of-plane OPC $\pm$  solutions may be left (-) or right (+) handed. The computed nonequilibrium chiral solutions have rotation numbers  $\Lambda = \pm 1$ , and the director rotates by  $2\pi$  rad when going from the bottom surface to the top surface; these solutions are similar to the equilibrium solutions of a cholesteric whose pitch is equal to the gap thickness. In the rest of this paper we only show all the (+) solution branches except where explicitly mentioned. A visualization of four (IP, OPN+, OPS+, OPC+) stationary solution types is shown in the last row of Table II.

We establish the bifurcation phenomena involved in branch switching and the parametric dependence of the four stationary branches discussed in this paper by constructing the bifurcation diagram [31,33,34]; the appropriate solution measures that capture the nonlinear phenomena are the centerline director components.

Figure 5 shows the bifurcation diagram in the three-dimensional space defined by  $(n_{x,\text{center}}, \mathcal{E}, n_{z,\text{center}})$ , for

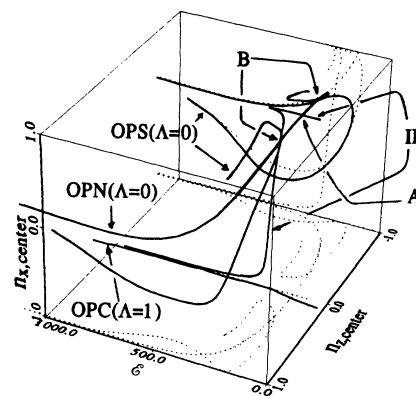


FIG. 5. Bifurcation diagram for the in-plane (IP) and out-of-plane (OP) orientation modes, for parallel anchoring, in three-dimensional space  $(n_{x,\text{center}}, n_{z,\text{center}}, \mathcal{E})$ . The solid lines are in the three-dimensional space. The dotted lines represent the orthogonal projections of the solid lines onto the zero tilt plane (bottom side of the box) and the zero twist plane (rear side of the box). The symbol  $A$  indicates the supercritical bifurcation point ( $\mathcal{E}_{co} = 148.6$ ) between IP and OPN branches. The symbol  $B$  indicates the transcritical bifurcation points ( $\mathcal{E}_{trs} = 159.1$ ) between OPN and OPS branches.

all the (+) and (-) branches. The solid lines are space curves, while the dotted lines are the projections of the solid lines onto  $(n_{x,\text{center}} = -1, \mathcal{E}, n_{z,\text{center}})$  and  $(n_{x,\text{center}}, \mathcal{E}, n_{z,\text{center}} = -1)$  planes. As described above, we find seven steady state solution branches, one in-shear-plane solution branch denoted as IP and three out-of-shear-plane solution branches denoted as OPN $\pm$  (twistable nematic), OPS $\pm$  (super-twistable nematic), and OPC $\pm$  (chiral nematic). The OPN $\pm$  and OPS $\pm$  are differentiated by their maximum twist angle:  $|\phi|_{\text{max}} = \pi/2$  rad is the maximum twist angle for the OPN $\pm$  branches, but  $|\phi|_{\text{max}}$  can exceed  $\pi/2$  rad for the OPS $\pm$  branches. The OPN $\pm$  branches emanates from a supercritical bifurcation at the point  $A(\mathcal{E}_{co}=148.6)$  on the IP solution branch, as shown in Fig. 5.

The bifurcation phenomena involving the various stationary solutions and the parametric ranges of multistability can be established by direct observation of Fig. 5; local stability was also confirmed by transient dynamic simulations. Figure 5 shows that the parametric space is divided into four representative regions:

- R<sub>1</sub>:  $0 < \mathcal{E} < \mathcal{E}_{tu}, \mathcal{E}_{tu} = 129.5$ ;
- R<sub>2</sub>:  $\mathcal{E}_{tu} < \mathcal{E} < \mathcal{E}_{co}, \mathcal{E}_{co} = 148.6$ ;
- R<sub>3</sub>:  $\mathcal{E}_{co} < \mathcal{E} < \mathcal{E}_{trs}, \mathcal{E}_{trs} = 159.1$ ;
- R<sub>4</sub>:  $\mathcal{E}_{trs} < \mathcal{E}$ .

The critical values of  $\mathcal{E}$  separating the four regions denote (a)  $\mathcal{E}_{tu}$ , turning points of the OPS $\pm$  branches;





(b)  $\mathcal{E}_{co}$ , a supercritical bifurcation point of the OPN $\pm$  branches from the IP branch; and (c)  $\mathcal{E}_{trs}$ . Transcritical bifurcation points involving the OPN $\pm$  and the OPS $\pm$  branches. The multistability in the four regions involve the following branches:

- R<sub>1</sub>: IP, OPC $\pm$ ;
- R<sub>2</sub>: IP, OPS $\pm$ , OPC $\pm$ ;
- R<sub>3</sub>: OPN $\pm$ , OPS $\pm$ , OPC $\pm$ ;
- R<sub>4</sub>: OPN $\pm$ , OPS $\pm$ , OPC $\pm$ .

Figure 5 shows that each branch of the OPS $\pm$  pair has, due to the presence of a turning point at  $\mathcal{E} = \mathcal{E}_{tu}$ , two different director structures, characterized by the magnitude of  $|n_{z,\text{center}}|$ . Dynamic simulations in R<sub>2</sub>, R<sub>3</sub>, and R<sub>4</sub> show that the OPS $\pm$  solutions with larger  $|n_{z,\text{center}}|$  are locally stable and that the solutions with smaller  $|n_{z,\text{center}}|$  are unstable.

The IP and OPN $\pm$  solutions have been previously predicted [27], and experimental evidence of this flow-induced instability involving a transition from the in-plane to the out-of-plane mode has been detected experimentally [19]. On the other hand, the OPS $\pm$  and OPC $\pm$  branches are predictions from the LE theory. The OPC $\pm$  solution branches are locally stable for all the  $\mathcal{E}$  values studied here and are not connected to any other branch. This shows that at relatively low  $\mathcal{E}$  ( $\mathcal{E} < \mathcal{E}_{tu}$ ) there is bistability involving the IP and OPC $\pm$  branches; similar bistability between in-plane and 180° twisted cells are

TABLE II. The orientation structure families at stable steady state for simple shear flow.

Orientation dimension	In-shear-plane 2D orientation	3D	3D	3D
Chirality	Achiral	Achiral	Achiral	Chiral
Rotation number ( $\Lambda$ )	0	0	0	$\pm 1$
Orientation structure	IP (In-plane)	OPN $\pm$ (twistable)	OPS $\pm$ (super-twistable)	OPC $\pm$ (cholesteric)
$ \phi _{\text{max}}$ (rad)	0	$\pi/2$	$\pi$	$2\pi$
$v_z(y)$ function	-	Odd	Odd	Even
Three-dimensional visualization of stable steady state orientation profile	IP 	OPN+ 	OPS+ 	OPC+ 

found in the presence of electromagnetic fields [35]. Using dynamic simulation we found that for  $\mathcal{E} > 430$ , the initial state is in the basin of attraction of the  $\text{OPC}\pm$  attractors, indicating that the initial monodomain texture undergoes a shear-induced transition from an achiral ( $\Lambda = 0$ ) mode into a chiral mode ( $\Lambda = \pm 1$ ). As shown below, this transition is irreversible with respect to flow reversal ( $U \rightarrow -U$ ) and to cessation of flow ( $U = 0$ ).  $\text{OPC}\pm$  solutions of higher rotation numbers ( $\Lambda = \pm n, n > 1$ ) have not been found. The rotation number  $\Lambda$  is an integer due to the fixed director anchoring. It is found to be independent of gap thickness, in accordance with Ericksen's scaling [36], which shows that two flow cells with driving velocities ( $U$ ) and gap thickness ( $h$ ), obeying

$$U_1 = \left(\frac{h_2}{h_1}\right)U_2, \quad (21)$$

display exactly the same scaled orientation and flow structure; this scaling holds for solutions belonging to the same branch. The initial efforts to understand the shear-flow of nonaligning nematics lead to the predictions of highly distorted in-plane solutions [37–40] and thus other twisted orientation modes were proposed but never computed [38]; these proposed textures, which appear to have been observed experimentally [41], are in qualitative agreement with the computed  $\text{OPC}\pm$  branches shown here.

The mirror symmetry displayed by the  $\text{OPN}\pm$ ,  $\text{OPS}\pm$ , and  $\text{OPC}\pm$  branches lead naturally to shear-induced periodic pattern-formation phenomena. In any unbiased sample, any of these textures displaying mirror symmetry are likely to be present in pairs, separated by mediating walls of in-plane mode; periodic textures produced by field-induced instabilities are usually present in nematic polymers [4–8] and flow-induced periodic textures in low molar mass nematics involving in-plane and out-of-plane modes have been thoroughly characterized experimentally [42] and theoretically [43,44].

## B. Orientation profile evolution

Figure 6(a) shows the centerline ( $y = h/2$ ) director evolution as a function of strain  $\gamma$  for  $\mathcal{E}=350.2$ , corresponding to the  $\text{OPS}+$  branch; the director components are shown as  $n_{x,\text{center}}$  (dashed line),  $n_{y,\text{center}}$  (solid line), and  $n_{z,\text{center}}$  (dotted line). After a dead strain  $\gamma_d \approx 120$ , a sharp change takes place. Figure 6(b) shows the corresponding splay (dotted line), twist (solid line), and bend (dashed line) energies per unit shearing area changing rapidly in that transition region. Each energy component is calculated by integration of Eq. (6). The magnitudes and times of sharp changes are scaled with the out-of-plane orientation transition, during which large splay and bend distortions occur first, followed by out-of-plane twist distortions. At long times the twist energy is the predominant component of the total Frank curvature energy, as expected for a twisted texture.

Figure 7(a) shows the evolution of the director components  $n_x$  (solid line) and  $n_z$  (dotted line) as a func-

tion of the strain  $\gamma$ , and the scaled thickness  $H = y/h$ . The corresponding visualization of the evolving texture is shown in Fig. 7(b). The initial director change involves in-plane tilting, while at latter times, combined tilting and twisting in the center line region results in a twisted  $\text{OP}$  steady state solution. At this shear rates, the time scales for tilting and twisting are similar, so that after an initial transient, the director's escape from the shear plane is concurrent with in-plane tilting. The orientation of the  $\text{OPS}\pm$  branches is characterized by the presence of twisting and an almost absence of in-plane tilting, in stark contrast to highly distorted IP plane solutions [37–40]. On the other hand, the orientation of the  $\text{OPN}\pm$  branches differ from that of the  $\text{OPS}\pm$  branches by the magnitude of the maximum twist angle, which is always less than  $\pi/2$  for the former but may be larger than  $\pi/2$  for the latter.

Figure 8(a) shows the centerline director components  $n_{x,\text{center}}$  (dashed line),  $n_{y,\text{center}}$  (solid line), and  $n_{z,\text{center}}$  (dotted line), as a function of strain  $\gamma$ , for the  $\text{OPC}+$  branch at  $\mathcal{E}=466.9$ . The step and pulse responses occur at a dead strain  $\gamma_d \approx 75$ , which indicates a much faster response than for the  $\text{OPN}+$  case [Fig. 6(a)] at a lower Ericksen number. The figure shows a rapid swing

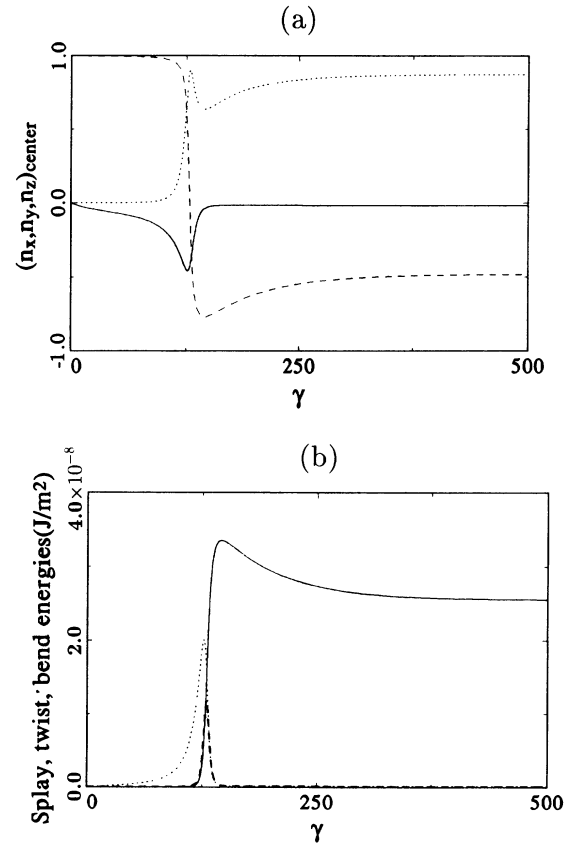


FIG. 6. Centerline director and Frank energy evolutions, for  $\mathcal{E}=350.2$ , corresponding to the  $\text{OPS}+$  branch. (a)  $n_{x,\text{center}}$  (dashed line),  $n_{y,\text{center}}$  (solid line), and  $n_{z,\text{center}}$  (dotted line) as functions of strain  $\gamma$ . (b) Frank energy evolutions of the splay (dotted line) mode, the twist (solid line) mode and the bend (dashed line) mode per unit shearing area ( $\text{J/m}^2$ ) as functions of strain  $\gamma$

of  $n_{x,\text{center}}$  from +1 to -1, but a small magnitude pulse in the  $n_{z,\text{center}}$ , indicating that, at the centerline, inplane tumbling is faster than out-of-plane twisting. Figure 8(b) shows the corresponding splay (dotted line), twist (solid line), and bend (dashed line) energies per unit shearing area. Again the pulse and step responses follow the director dynamics, which eventually lead to a predominantly twist contribution at steady state, as expected for a chiral nematic.

Figure 9(a) shows the evolution of the corresponding  $n_x$  (solid line) and  $n_z$  (dotted line) director components as a function of strain  $\gamma$  and scaled thickness  $H = y/h$ . The figure shows that  $n_x$  has an even flat wall profile but  $n_z$  has an odd profile with a pair of peaks close to the boundaries, indicating that the orientation is inplane at the centerline region but out-of-plane close to the walls, in agreement with experimental measurement [19]. Figure 9(b) shows the corresponding visualization of the achiral to chiral nematic transition. The figure shows that at the centerline, in-plane tilting is faster than out-

of-plane twisting, which eventually leads to a defect-free nucleation of a chiral texture having a full  $2\pi$  director rotation. This orientation texture is similar to that of a monodomain cholesteric liquid crystal at equilibrium between two flat plates, whose separation is equal to the pitch, and can be experimentally detected because of its distinct optical properties [45–47]. The achiral ( $\Lambda = 0$ ) to chiral transition ( $\Lambda = \pm 1$ ) involves no singularities since the two director profiles are topologically equivalent and can be mapped into each other by a nonsingular transformation.

The instability mechanism can be established by a torque analysis. The OP twisting and IP tilting viscous torques due to the primary velocity acting on the director are, respectively,

$$\Gamma_{y^*}^v = -\frac{\gamma_2}{4} \frac{\partial v_x}{\partial y} \sin 2\phi \sin 2\theta, \quad (22)$$

$$\Gamma_{z^*}^v = \frac{\partial v_x}{\partial y} \left( -\gamma_1 - \frac{\gamma_2 \cos 2\theta \cos \phi}{2} \right), \quad (23)$$

where  $\phi$  and  $\theta$  are defined in Fig. 1; the torque axis  $y^*$  is orthogonal to  $\mathbf{n}$  and in the shear plane while the  $z^*$  axis is normal to the  $\mathbf{n}$ - $y^*$  plane [27]. A comparison of the

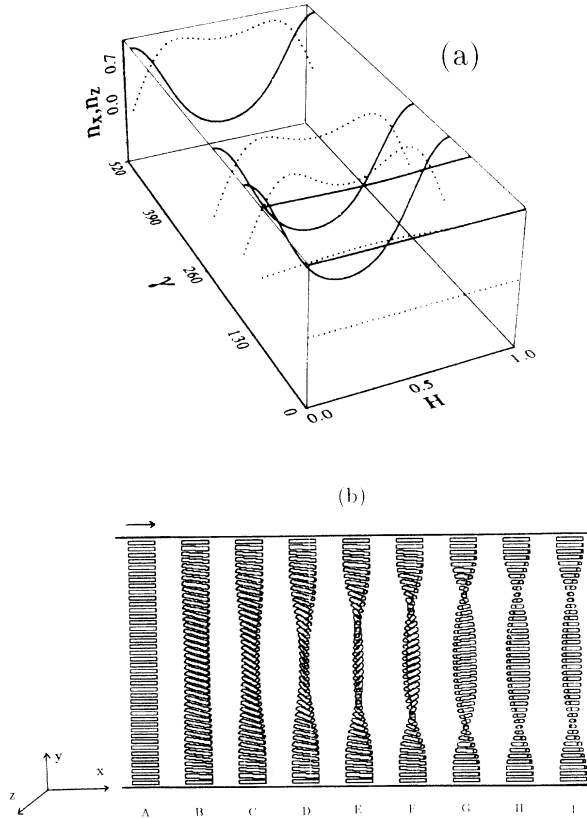


FIG. 7. (a) Box plots of the director profile evolution for  $\mathcal{E}=350.2$ , corresponding to OPS+ branch.  $n_x$  profiles (solid lines) and  $n_z$  profiles (dotted lines) as functions of the dimensionless thickness ( $H = y/h$ ) and strain  $\gamma$ . (b) Three-dimensional visualization of the structure evolution. Each visualization corresponds to the following strain  $\gamma$ : A=0.0, B=121.8, C=126.0, D=127.9, E=129.9, F=132.0, G=138.7, H=157.4, and I=238.46.

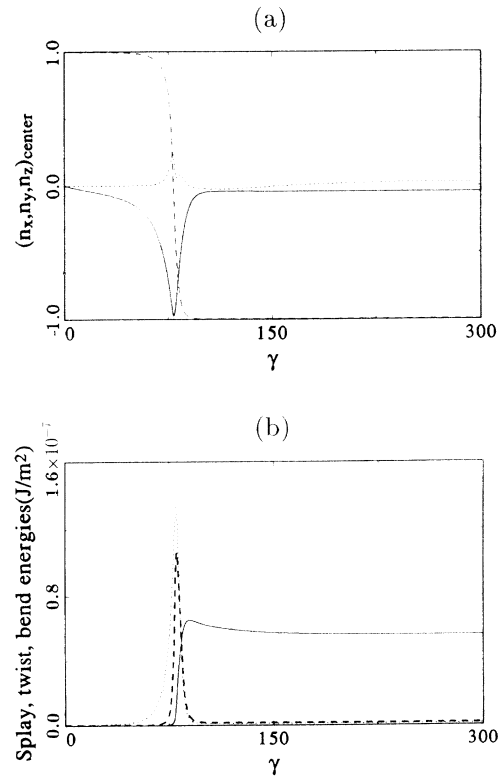


FIG. 8. (a) Centerline director and Frank energy evolutions, for  $\mathcal{E}=466.9$ , corresponding to the OPC+ branch; (a)  $n_{x,\text{center}}$  (dashed line),  $n_{y,\text{center}}$  (solid line), and  $n_{z,\text{center}}$  (dotted line) as functions of strain unit  $\gamma$ . (b) Frank energy evolutions of the splay mode (dotted line), the twist mode (solid line), and the bend mode (dashed line) per unit shearing area ( $\text{J}/\text{m}^2$ ), as functions of strain  $\gamma$ .



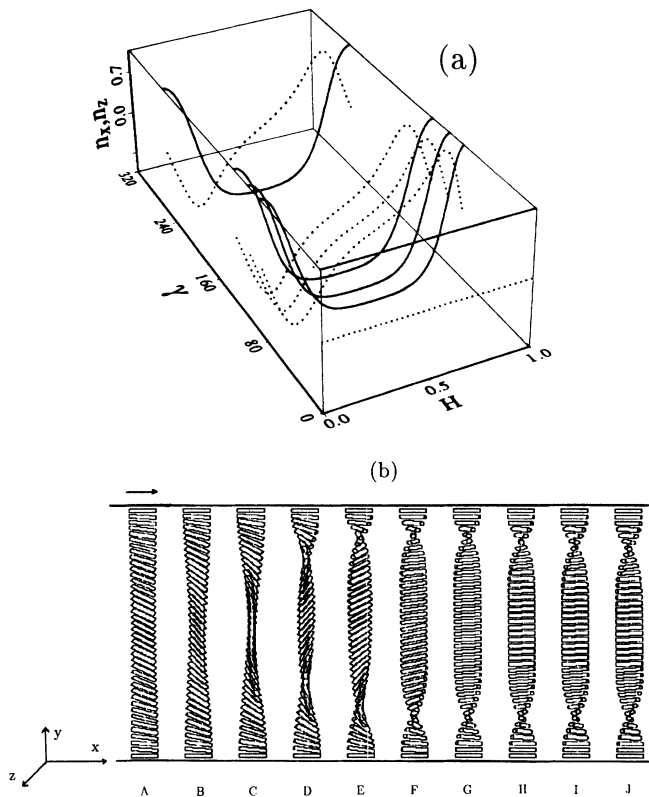


FIG. 9. (a) Box plots of the director profile evolution for  $\mathcal{E}=466.9$ , corresponding to the OPC+ branch.  $n_x$  profiles (solid lines) and  $n_z$  profiles (dotted lines) as functions of the dimensionless thickness ( $H = y/h$ ) and strain  $\gamma$ . (b) Three-dimensional visualizations of the director evolution for  $\mathcal{E}=466.9$ . Each director visualization corresponds to the following strain  $\gamma$ : A=72.69, B=76.86, C=78.36, D=80.20, E=82.18, F=87.37, G=92.78, H=105.9, I=128.7, and J=252.9.

relative magnitudes of these two torques lead to the identification of the instability mechanism, since the OPN $\pm$  and OPS $\pm$  branches are favored when  $\Gamma_{z*}^v \ll \Gamma_{y*}^v$  at the center region, while the OPC $\pm$  branches are favored when  $\Gamma_{z*}^v \ll \Gamma_{y*}^v$  at the two wall regions. Assuming an initial in-plane orientation, the extrema of the strengths of the viscous torques, as the director samples the fourth quadrant, are a minimum for the IP tilting torque, and a maximum for the OP twisting torque at  $\theta = -\pi/4$ , which coincides with the compression direction of shear. At relatively low  $\mathcal{E}$ , where the achiral modes are favored, the director tilting speed is slow and any out-of-plane fluctuation has time to grow as it enters the compression region, thus leading to the one way uniformly twisted, out-of-plane modes ( $\mathcal{E}$  must be larger than  $\mathcal{E}_{co}$  so that the driving  $\Gamma_{y*}^v$  torques overcome the stabilizing elastic torques; see [27]). On the other hand, at relatively higher  $\mathcal{E}$ , the tilting speed at the centerline is faster than at the bounding surface, so that the core tumbles past the compression axes ( $-\pi/4$ ) without twisting, but at the two wall regions the slow tilting allows for a director escape from the shear plane.

### C. Velocity profile evolution and particle tracking visualization

Figure 10(a) shows the evolution of the primary velocity ( $U_x = v_x/U$ ) profile (solid line) and of the secondary velocity ( $U_z = v_z/U$ ) profile (dotted line) as functions of dimensionless thickness ( $H = y/h$ ), for  $\mathcal{E}=350.2$ , corresponding to the OPS+ mode. For small strains ( $\gamma$ ) the primary velocity profile is linear, but becomes sigmoidal at larger strains, in agreement with experimentally observed flow visualizations [48]; the nonlinearity reflects the director's escape from the shear plane. The figure shows that the magnitude of the secondary velocity increases at the transition and that the net secondary velocity is zero;  $U_z$  is an odd function of  $H$ .

Figure 10(b) shows the velocity profile evolutions for the achiral to chiral nematic transition, for  $\mathcal{E}=466.9$ . The primary velocity profile (solid line) readily becomes nonlinear at small strains due to the faster IP tilting. There are two inflection points in the steady state primary velocity profile off the center region, but these two are more separated than the achiral orientation case. The sec-

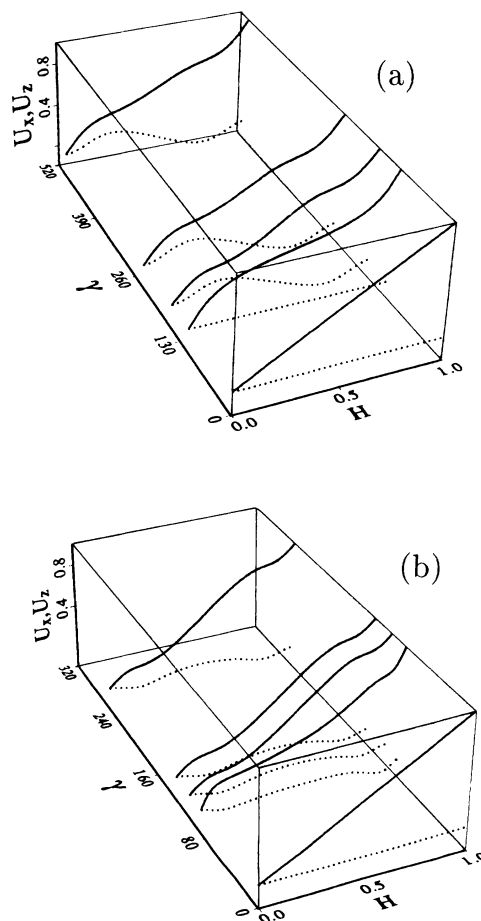


FIG. 10. (a) Evolution of the primary velocity ( $v_x = v_x/U$ ) profile (solid line) and the secondary velocity ( $U_z = v_z/U$ ) profile (dotted line) as functions of dimensionless thickness ( $H = y/h$ ), for  $\mathcal{E}=350.2$ , corresponding to the OPS+ branch. (b) Velocity evolutions for the achiral-chiral nematic transition, for  $\mathcal{E}=466.9$ .

ondary velocity profile (dotted line) undergoes complex slow oscillation in the transition range and its magnitude decreases at the steady state. The secondary velocity is smaller than that of the OPS± case due to the less overall out-of-shear-plane orientation. The net secondary flow is zero.

Particle tracking experiments that show the trajectory  $(x(y, t), z(y, t))$  of the nematic fluid elements can be visualized from the dynamic simulation results using the following equations:

$$x(y, t) = \int_0^t v_x(y, t) dt, \quad z(y, t) = \int_0^t v_z(y, t) dt, \quad (24)$$

where  $x$  and  $z$  denote the particle Lagrangian coordinates. Figures 11 and 12 show the particle trajectories corresponding to the OPS± and OPC± orientation texture evolutions for small (weakly nonlinear response)

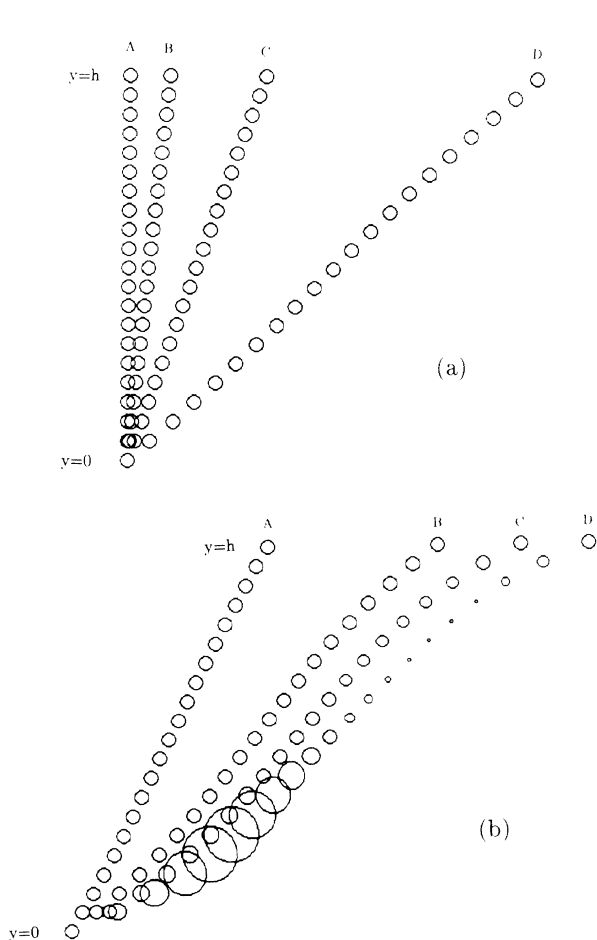


FIG. 11. Particle tracking images for  $\mathcal{E}=350.2$ , corresponding to the OPS+ branch. The size of the circle scales with the distance from the viewer: the smaller the circle the further away it is from the viewer, and vice versa. (a) Small strain (early time) stage. The maximum upper plate displacement is  $2.026 \times 10^{-2}$  m; the corresponding strains are  $A=0.0$ ,  $B=5.761$ ,  $C=19.243$ , and  $D=57.89$ . (b) Large strain (late time) stage. The maximum upper plate displacement is  $5.228 \times 10^{-2}$  m; the corresponding strains are  $A=57.89$ ,  $B=106.2$ ,  $C=130.12$ , and  $D=149.37$ .

and large (nonlinear response) strain stages, respectively. The radius of the particle represents how far away the particle is from the observer, which views the shear plane from the neutral axes ( $z$ ); the smaller the particle, the further away it is from the observer, and vice versa. For the small strain stage, the curve connecting the particles at the same time shows which is in good agreement with the experimental observations [48]. As more strains are applied, the path lines are reminiscent of those experimentally observed when a nematic polymer is subjected to an orienting magnetic field [19].

In summary we have found that (i) for the OP modes, the initially linear primary velocity profile becomes highly nonlinear at the steady state, (ii) orientation induces secondary flows whose relative magnitude to the primary flows are larger for the OPS± branches than for OPC± branches, and (iii) particle tracking visualizations show complex nonlinear path lines.

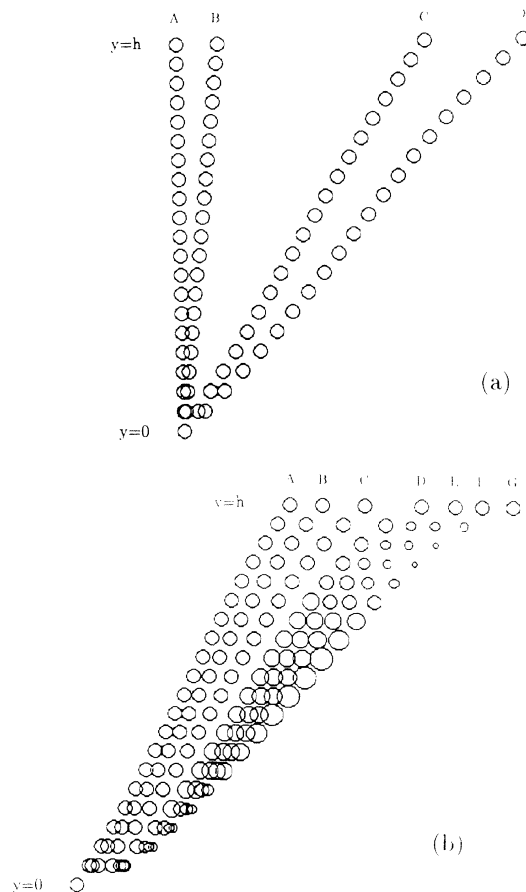


FIG. 12. Particle tracking images for  $\mathcal{E}=466.9$ , corresponding to the OPC+ branch. The size of the circle denotes distance from the viewer: the smaller the circle the further away it is from the viewer, and vice versa. (a) Small strains (early time) stage. The maximum upper plate displacement is  $1.726 \times 10^{-2}$  m; the corresponding strains are  $A=0.0$ ,  $B=5.877$ ,  $C=35.24$ , and  $D=49.32$ . (b) Large strains (late time) stage. The maximum upper plate displacement is  $3.577 \times 10^{-2}$  m; the corresponding strains are  $A=49.32$ ,  $B=56.81$ ,  $C=66.99$ ,  $D=80.26$ ,  $E=88.31$ ,  $F=94.71$ , and  $G=102.20$ .

### D. Rheological function evolution

Rheology is a useful tool to characterize and classify materials [49]. Here we use two characteristic rheological functions, the apparent viscosity  $\eta_{\text{app}}$  and the first normal stress difference  $N_1$  defined by

$$\eta_{\text{app}} = \frac{\sigma_{xy,w}}{\dot{\gamma}_n}, \quad N_1 = \sigma_{xx,w} - \sigma_{yy,w}, \quad (25)$$

where  $\sigma_{xy,w}, \sigma_{xx,w}, \sigma_{yy,w}$  are the wall stresses and  $\dot{\gamma}_n$  is the nominal shear rate ( $U/h$ ). Figure 13(a) shows the apparent viscosity (dotted line) and the first normal stress difference (solid line), as a function of strain, for  $\mathcal{E}=350.2$ , corresponding to the OPS+ branch. The apparent viscosity evolution shows one overshoot followed by a slight undershoot, and the first normal stress evolution shows two overshoots. The first normal stress response is more pronounced than the apparent viscosity response, and this difference is more apparent as  $\mathcal{E}$  increases. Figure 13(b) shows the apparent viscosity (dotted line) and the first normal stress difference (solid line) evolutions for the achiral-chiral transition, when  $\mathcal{E}=466.9$ . The apparent viscosity levels off more quickly, after one overshoot.

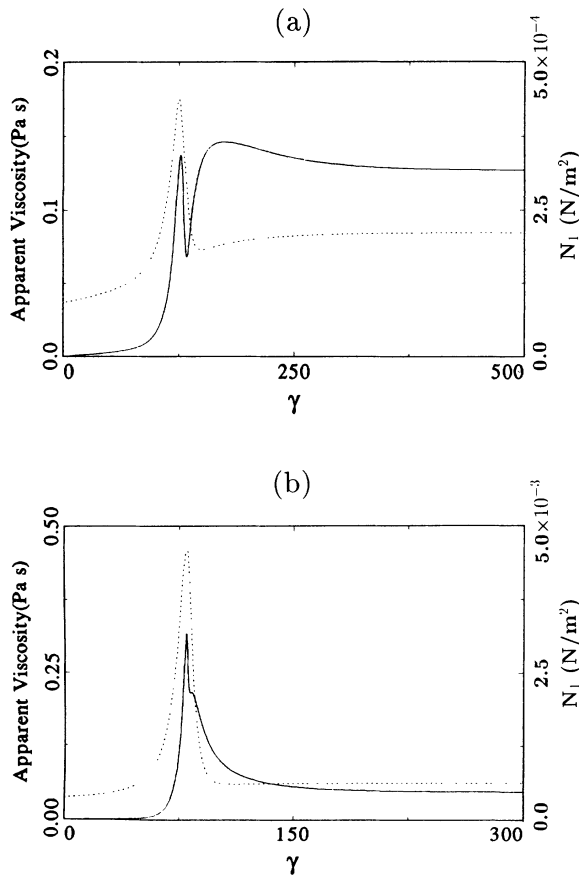


FIG. 13. Characterization of the rheological response to shear start-up flow. Apparent viscosity  $\eta$  (Pa s) (dotted line) and the first normal stress difference  $N_1$  (Pa) (solid line) as functions of strain  $\gamma$ . (a)  $\mathcal{E}=350.6$ , corresponding to the OPS+ branch; (b)  $\mathcal{E}=466.9$ , corresponding to the OPC+ branch.

Since the orientation evolution is quicker than that of the achiral orientation case shown above, the shear stress response time is accordingly shorter. The first normal stress shows one peak with a small kink, and this kink grows as a second overshoot, introducing more oscillatory behavior with increasing  $\mathcal{E}$ . Also, we notice a decreasing viscosity with increasing Ericksen number, which is typical for shear-thinning fluids.

Comparisons between Figs. 13(a) and 6(a) and between 13(b) and 8(a) show that the peaks of overshoots and undershoots of the rheological functions are caused by the structural changes in the director evolution. The characteristic changes in the rheological functions do not scale exactly with the strain since evolutions leading to the OPS and OPC solutions have different orientation time constants  $\tau_0$ . The orientation time constant  $\tau_0 = \gamma_1 h^2 / K_{\text{eff}}$  depends on the effective Frank elasticity  $K_{\text{eff}}$ , which scales with the Frank free energy density; a comparison between Figs. 6(b) and 8(b) shows that the  $\tau_0$  for the OPS mode is higher than the  $\tau_0$  for the OPC mode and therefore the strains corresponding the characteristic rheological changes are smaller for the OPC mode than for the OPS mode.

In summary we have found that (i) shear start-up flow produces underdamped and large oscillatory rheological responses such as those experimentally observed for nematic polymers [20,50–54], (ii) as  $\mathcal{E}$  increases the rheological responses become faster due to faster orientational change, and (iii) in contrast to isotropic, viscous, and viscoelastic polymeric fluids, nonlinear behavior is predicted even at low shear rates. For isotropic flexible polymers nonlinear behavior exists at shear rates several decades higher than those studied here, since these fluids do not exhibit any significant structural changes at low shear rates.

### E. Phase stability diagram, multistability, and basins of attraction

In this section we present the stability diagram, further identify the parametric regions of solution multistability, and determine the parametric dependence of the basins of attractions of the various stable steady state solutions.

Figure 14 shows the stability diagram, given by  $2|\Lambda| + n_{x,\text{center}}$  as a function of the Ericksen number  $\mathcal{E}$ ; the magnitude of revolution number  $|\Lambda|$  provides the required classifying index. The ordinate of Figs. 14 and 15 was chosen such that the set of three-dimensional stability curves on the  $(|\Lambda|, \mathcal{E}, n_{x,\text{center}})$  space can be effectively reduced, by a projection and translation, to the shown two-dimensional curves. The upper boundary of the plane corresponds to chiral ( $\Lambda = \pm 1$ ) solutions, and the plane itself corresponds to the achiral ( $\Lambda = 0$ ) solutions; the dash-dotted line represents the OPN $\pm$  branches, the dotted line the IP branch, the solid line the OPC $\pm$  branches, and the dashed line the OPS $\pm$  branches. The filled arrowheads represents (a) a turning point on the IP branch, (b) a supercritical bifurcation point between the IP and OPN $\pm$  branches, (c) a transcritical bifurcation point between the OPN $\pm$  and OPS $\pm$  branches, and (d) a turning

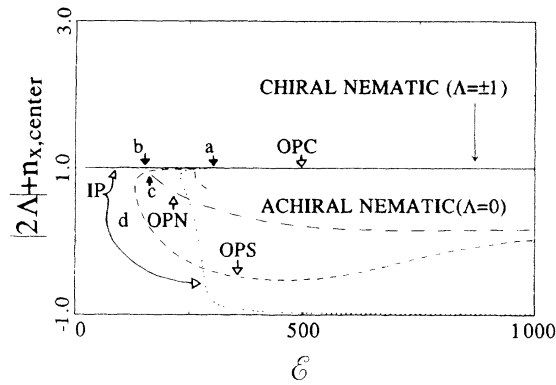


FIG. 14. Stability phase diagram of simple shear flow for a model nematic polymer (PBG) at steady state.  $\Lambda$  is the quantized number of director twist revolutions. The dotted, dot-dashed, dashed, and solid lines represent the IP, OPN $\pm$ , OPS $\pm$ , and OPC $\pm$  orientation structures, respectively. The filled arrow heads next to the lower case letter (a–d) represents, for increasing  $\mathcal{E}$  values, a turning point of OPS the branch (d), a supercritical bifurcation point between the IP and OPN $\pm$  branches (b), a transcritical branch between the OPN $\pm$  and OPS $\pm$  branches (c), and a turning point in the IP branch (a).

point on the OPS $\pm$  branch.

The specific values of  $\mathcal{E}$  at which bifurcations occur and the local stability properties of the solutions were given in Sec. III A. Given any  $\mathcal{E}$  the diagram provides information on the chirality of the locally stable solutions. The solution multiplicities shown in Fig. 14 and quoted in Sec. III A lead to the selection problem of

coexisting steady state attractors. Each attractors has a basin of attraction, defined as the subset of initial data  $\mathbf{I}^0(\mathbf{v}(0, y), \mathbf{n}(0, y))$  with the property  $\mathcal{L}(t, \mathbf{I}^0) \rightarrow \mathbf{I}_s$  as  $t \rightarrow +\infty$ , where  $\mathbf{I}_s = (\mathbf{v}_s(y), \mathbf{n}_s(y))$  are the locally stable steady states. Here  $\mathbf{I}^0$  is fixed, and we wish to establish the parametric dependence of the boundaries between basins with respect to the given  $\mathbf{I}^0$ , that is, which steady state is adopted when the sample is suddenly driven with a given value of  $\mathcal{E}$ . The parametric range of the adopted steady states, or basin location of  $\mathbf{I}^0$ , obtained from dynamic simulations are

- (i)  $0 < \mathcal{E} < \mathcal{E}_{co} = 148.6$  (IP mode),
- (ii)  $\mathcal{E}_{co} < \mathcal{E} < \mathcal{E}_{ns} = 300$  (OPN $\pm$  modes),
- (iii)  $\mathcal{E}_{ns} < \mathcal{E} < \mathcal{E}_{sc} = 430$  (OPS $\pm$  modes),
- (iv)  $\mathcal{E}_{sc} < \mathcal{E}$  (OPC $\pm$  modes).

The information is summarized in Fig. 15, which shows the orientation mode selection diagram when a sample at rest is driven with a constant  $\mathcal{E}$ .

#### F. Irreversality and history dependence of the stable steady-state structures

In this section we first show the irreversible nature of the achiral to chiral orientation transition by simulating relaxation after cessation of flow, and flow reversal. In the former simulation the upper plate velocity is suddenly set to zero, and in the latter it is suddenly switched from  $+U$  to  $-U$ . Finally, history dependent orientation mode selections are shown.

Figure 16 shows the three-dimensional visualization of the structure evolution after stopping the flow. The ori-

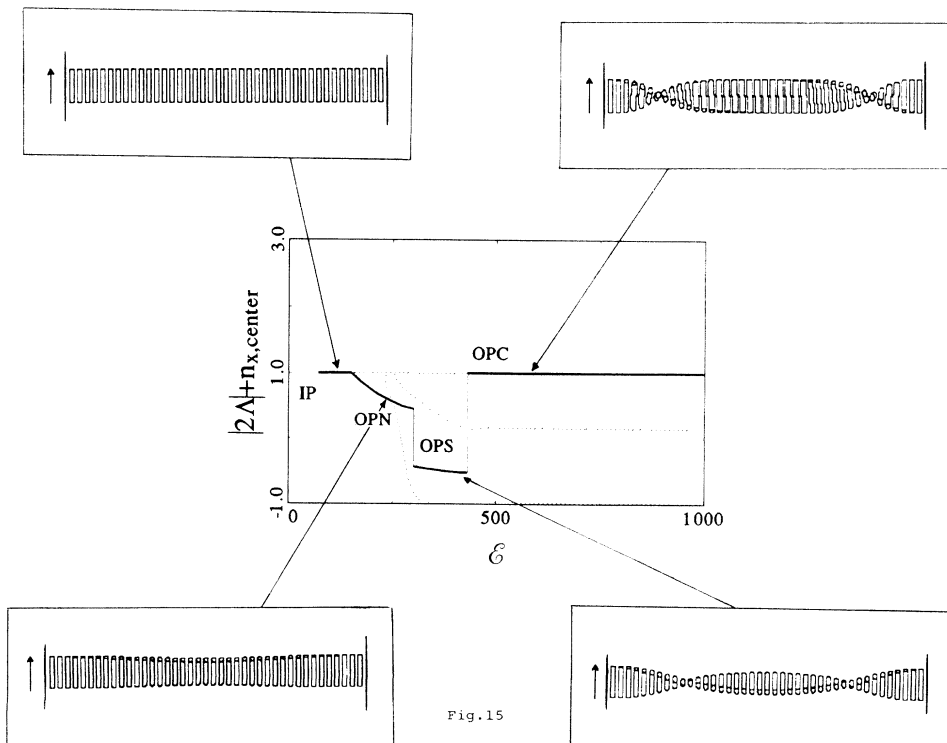


FIG. 15. Orientation mode selection diagram for shearing at constant  $\mathcal{E}$ ;  $\Lambda$  is the quantized number of director twist revolutions. The bold solid line segments represent the selected steady state IP, OPN, OPS, and OPC modes, and the inserts contain representative visualization for the four modes.

Fig. 15

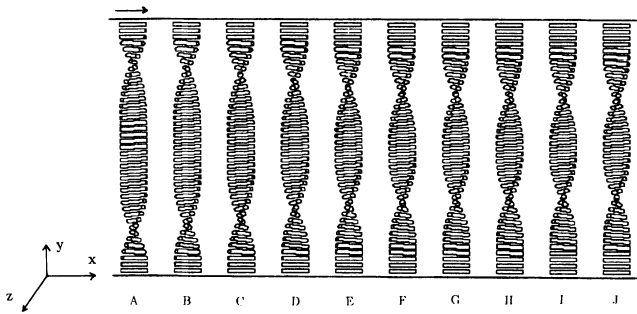


FIG. 16. Three-dimensional visualizations of the director evolutions after cessation of steady shear flow (from  $\mathcal{E}=466.9$  to  $\mathcal{E}=0.0$ ). The corresponding times (sec), after the cessation of steady flow, are  $A=8.514 \times 10^2$ ,  $B=4.878 \times 10^3$ ,  $C=9.072 \times 10^3$ ,  $D=1.673 \times 10^4$ ,  $E=2.478 \times 10^4$ ,  $F=3.317 \times 10^4$ ,  $G=4.123 \times 10^4$ ,  $H=5.052 \times 10^4$ ,  $I=6.663 \times 10^4$ , and  $J=1.034 \times 10^5$ .

entation helix relaxes from the nonuniform helix towards the regular helix, like a regular helical spring, which is forced to have nonuniform twist. During the relaxation, the orientation profiles slowly lose symmetry by moving the initially in-plane orientation wall off the center. The irreversibility of the chiral orientation is due to the anisotropy in the Frank elastic constant; Table I shows that the twist constant  $K_{22}$  is significantly smaller than the splay  $K_{11}$  and bend  $K_{33}$  constants. To restore the achiral nematic mode, the director must go through large splay-bend distortions, as shown in Fig. 9(b); transient simulations show that reversibility to the achiral mode is only possible for nearly isotropic Frank elasticity. Two types of shear-flow-induced transitions, reversible and irreversible orientation transitions, have been experimentally observed [55–57], which may suggest that the predicted transitions shown here can also be detected.

Figure 17 shows the three-dimensional visualization of the orientation evolution upon flow reversal. Again, the original achiral nematic structure is not recovered, and the net result of the reversal is a small adjustment in the director orientation.

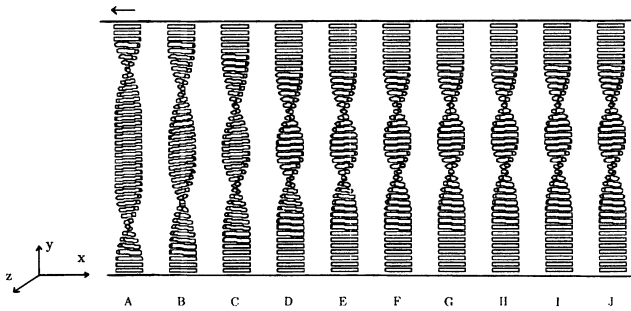


FIG. 17. Three-dimensional visualizations of director evolutions for flow reversal (from  $\mathcal{E}=466.9$  to  $\mathcal{E}=-466.9$ ). The corresponding strains  $\gamma$ , after the flow reversal, are  $A=-4.180$ ,  $B=1.338 \times 10^1$ ,  $C=-2.452 \times 10^1$ ,  $D=-6.659 \times 10^1$ ,  $E=-1.770 \times 10^2$ ,  $F=-4.409 \times 10^2$ ,  $G=-8.182 \times 10^2$ ,  $H=-1.338 \times 10^3$ ,  $I=-2.900 \times 10^3$ , and  $J=-4.357 \times 10^4$ .

The dependence of the stable steady states to sample preparation (strain history) is another evidence of the nonlinear dynamics exhibited by this system and the invalidity of the linear superposition principle [58]. Here we show that three different steady state textures  $\{T_i$  ( $i = A, B, C$ )} are obtained from the same initial texture  $T(0)$ , the same final  $\mathcal{E} = \mathcal{E}^*$ , but three different intermediate deformation histories  $\{\mathcal{E}_i(\gamma), i = A, B, C\}$ . Figure 18(a) shows three different sample preparations leading to three different stable steady state solution branches for  $\mathcal{E}^* = 467$ : path A,  $\mathcal{E}_A = 467H(\gamma)$ ; path B,  $\mathcal{E}_B = 350H(\gamma) + 117H(\gamma - 150)$ ; and path C,  $\mathcal{E}_C = 233H(\gamma) + 234H(\gamma - 600)$ , where  $H(\gamma)$  is the Heaviside unit step function. The visualizations of the corresponding stable steady director orientations are shown in Fig. 18(b). The figure shows that even if  $\mathcal{E}^* = 467$  in all cases, path A leads to the OPC+ branch, path B to the OPS+ branch, and path C to the OPN+ branch. These observations confirm the importance of sample preparation in the study of nonlinear systems.

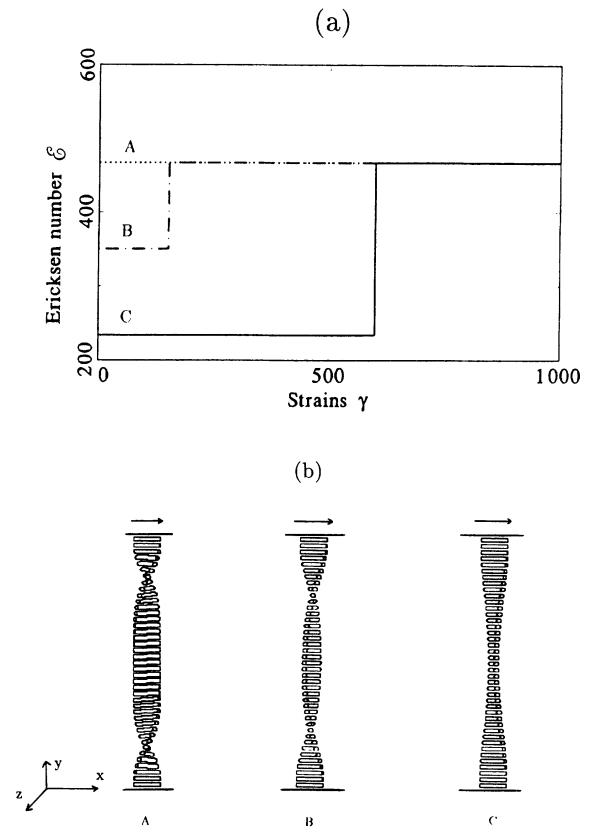


FIG. 18. Dependence of the steady orientation mode selection on the Ericksen number history. (a) Three different Ericksen number histories  $\{\mathcal{E}_i(\gamma), i = A, B, C\}$  as a function of strain,  $\mathcal{E}_A = 467H(\gamma)$ ,  $\mathcal{E}_B = 350H(\gamma) + 117H(\gamma - 150)$ , and  $\mathcal{E}_C = 233H(\gamma) + 234H(\gamma - 600)$ ;  $H(\gamma)$  is the Heaviside unit step function. (b) Three-dimensional visualizations of adopted stable steady-state orientation structures. Path A eventually leads to the chiral orientation structure (OPC+), path B to the supertwistable orientation structure (OPS+), and path C to the twisted orientation structure (OPN+).

#### IV. CONCLUSIONS

An efficient numerical adaptive method to solve the Leslie-Ericksen equation for nematics, displaying complex three-dimensional orientation, has been presented and applied in conjunction with computational bifurcation methods to the transient and steady rectilinear simple shear flow. The parameter that controls the main microstructural features and stability properties of the flow is the Ericksen number. For the range of studied  $\mathcal{E}$  values, seven steady state solutions were found, six of which are characterized by three-dimensional orientation (OPS $\pm$ , OPN $\pm$ , OPC $\pm$ ); these six solutions are three pairs of dissipatively equivalent mirror images of each other. Four solutions (OPS $\pm$ , OPN $\pm$ ) are characterized by one-way twist deformations, while the two OPC $\pm$  branches are chiral nematics, displaying one full director rotation when going from one surface to the other. All the seven solutions are attainable by different appropriate shearing histories of the some initial monodomain orientation. The characterized nonlinear phenomena include supercritical and transcritical bifurcations, turning points, multistability, nonlinear strains, secondary flows, non-Newtonian rheology, and strong history dependence of stable steady state textures. Bifurcations in the presence of symmetry give rise to left or right twisted achiral

solutions and left or right handed chiral solutions. Both solutions in each pair are dissipatively equivalent and both should therefore be observed in an unbiased flow cell. Thus the bifurcation in the presence of symmetry shown here naturally leads to typical periodic textures consisting of alternating (+) or (-) out-of-plane modes separated by mediating walls of in-plane solutions.

#### ACKNOWLEDGMENTS

This work is supported by a research grant from Natural Science and Engineering Research Council of Canada. W.H.H. would like to thank the Government of the Republic of Korea for financial support.

#### APPENDIX: THE LINEAR MOMENTUM AND TORQUE BALANCES

The full Leslie-Ericksen equations with orientation structure embedded torque balance equations for simple shear flow is obtained using the symbolic manipulation programming language MATHEMATICA [32]. There is no body force and only the gradients along the thickness direction are considered.

##### 1. x-momentum balance

$$\begin{aligned}
& \rho \frac{\partial v_x}{\partial t} - \alpha_2 n_y \frac{\partial^2 n_x}{\partial t \partial y} - \alpha_3 \frac{\partial n_x}{\partial y} \frac{\partial n_y}{\partial t} - \alpha_2 \frac{\partial n_x}{\partial t} \frac{\partial n_y}{\partial y} - \alpha_3 n_x \frac{\partial^2 n_y}{\partial t \partial y} \\
&= \left( \frac{\partial n_x}{\partial y} (\alpha_3 n_x + \alpha_6 n_x + 2\alpha_1 n_x n_y^2) + [-(\alpha_2 n_y) + \alpha_5 n_y + 2\alpha_1 n_x^2 n_y] \frac{\partial n_y}{\partial y} \right) \frac{\partial v_x}{\partial y} \\
&+ (\alpha_4/2 + \alpha_3 n_x^2/2 + \alpha_6 n_x^2/2 - \alpha_2 n_y^2/2 + \alpha_5 n_y^2/2 + \alpha_1 n_x^2 n_y^2) \frac{\partial^2 v_x}{\partial y^2} \\
&+ \left( 2\alpha_1 n_x n_y \frac{\partial n_y}{\partial y} n_z + \frac{\partial n_x}{\partial y} (\alpha_3 n_z/2 + \alpha_6 n_z/2 + \alpha_1 n_y^2 n_z) + (\alpha_3 n_x/2 + \alpha_6 n_x/2 + \alpha_1 n_x n_y^2) \frac{\partial n_z}{\partial y} \right) \frac{\partial v_z}{\partial y} \\
&+ (\alpha_3 n_x n_z/2 + \alpha_6 n_x n_z/2 + \alpha_1 n_x n_y^2 n_z) \frac{\partial^2 v_z}{\partial y^2}. \tag{A1}
\end{aligned}$$

##### 2. z-momentum balance

$$\begin{aligned}
& \rho \frac{\partial v_z}{\partial t} - \alpha_3 n_z \frac{\partial^2 n_y}{\partial t \partial y} - \alpha_2 \frac{\partial n_y}{\partial y} \frac{\partial n_z}{\partial t} - \alpha_3 \frac{\partial n_y}{\partial t} \frac{\partial n_z}{\partial y} - \alpha_2 n_y \frac{\partial^2 n_z}{\partial t \partial y} \\
&= \left( 2\alpha_1 n_x n_y \frac{\partial n_y}{\partial y} n_z + \frac{\partial n_x}{\partial y} (\alpha_3 n_z/2 + \alpha_6 n_z/2 + \alpha_1 n_y^2 n_z) + (\alpha_3 n_x/2 + \alpha_6 n_x/2 + \alpha_1 n_x n_y^2) \frac{\partial n_z}{\partial y} \right) \frac{\partial v_x}{\partial y} \\
&+ (\alpha_3 n_x n_z/2 + \alpha_6 n_x n_z/2 + \alpha_1 n_x n_y^2 n_z) \frac{\partial^2 v_x}{\partial y^2} + \left( \frac{\partial n_y}{\partial y} [-(\alpha_2 n_y) + \alpha_5 n_y + 2\alpha_1 n_y n_z^2] \right. \\
&+ (\alpha_3 n_z + \alpha_6 n_z + 2\alpha_1 n_y^2 n_z) \frac{\partial n_z}{\partial y} \left. \right) \frac{\partial v_z}{\partial y} + (\alpha_4/2 - \alpha_2 n_y^2/2 + \alpha_5 n_y^2/2 + \alpha_3 n_z^2/2 + \alpha_6 n_z^2/2 + \alpha_1 n_y^2 n_z^2) \frac{\partial^2 v_z}{\partial y^2}. \tag{A2}
\end{aligned}$$

3.  $g_1$ -torque balance

$$\begin{aligned}
& -\gamma_1 [-(n_y g_{1x}^*) + n_x g_{1y}^*] \frac{\partial n_z}{\partial t} + \frac{\partial n_y}{\partial t} (n_z g_{1x}^* - n_x g_{1z}^*) + \frac{\partial n_x}{\partial t} [-(n_z g_{1y}^*) + n_y g_{1z}^*] \\
& = K_{11} \frac{\partial^2 n_y}{\partial y^2} [-(n_z g_{1x}^*) + n_x g_{1z}^*] + \gamma_1 \left( n_x n_z \frac{\partial v_x}{\partial y} g_{1x}^*/2 + n_y^2 \frac{\partial v_z}{\partial y} g_{1x}^*/2 + n_z^2 \frac{\partial v_z}{\partial y} g_{1x}^*/2 \right. \\
& \quad \left. + n_y n_z \frac{\partial v_x}{\partial y} g_{1y}^*/2 - n_x n_y \frac{\partial v_z}{\partial y} g_{1y}^*/2 - n_x^2 \frac{\partial v_x}{\partial y} g_{1z}^*/2 - n_y^2 \frac{\partial v_x}{\partial y} g_{1z}^*/2 - n_x n_z \frac{\partial v_z}{\partial y} g_{1z}^*/2 \right) \\
& \quad + \gamma_2 \left( n_x n_z \frac{\partial v_x}{\partial y} g_{1x}^*/2 - n_y^2 \frac{\partial v_z}{\partial y} g_{1x}^*/2 + n_z^2 \frac{\partial v_z}{\partial y} g_{1x}^*/2 - n_y n_z \frac{\partial v_x}{\partial y} g_{1y}^*/2 + n_x n_y \frac{\partial v_z}{\partial y} g_{1y}^*/2 - n_x^2 \frac{\partial v_x}{\partial y} g_{1z}^*/2 \right. \\
& \quad \left. + n_y^2 \frac{\partial v_x}{\partial y} g_{1z}^*/2 - n_x n_z \frac{\partial v_z}{\partial y} g_{1z}^*/2 \right) + K_{33} \left( \frac{\partial n_y}{\partial y} \frac{\partial n_z}{\partial y} (2n_y^2 g_{1x}^* - 2n_x n_y g_{1y}^*) \right. \\
& \quad \left. + \frac{\partial^2 n_z}{\partial y^2} (n_y^3 g_{1x}^* - n_x n_y^2 g_{1y}^*) + \frac{\partial n_x}{\partial y} (n_y n_z g_{1x}^* - n_x n_y g_{1z}^*) \right. \\
& \quad \left. + \frac{\partial n_z}{\partial y} (n_y n_z g_{1x}^* - n_x n_y g_{1z}^*) + \frac{\partial n_y}{\partial y} [-(n_y n_z g_{1x}^*) + n_x n_y g_{1z}^*] \right. \\
& \quad \left. + \frac{\partial n_x}{\partial y} \frac{\partial n_y}{\partial y} (2n_y n_z g_{1y}^* - 2n_y^2 g_{1z}^*) \right. \\
& \quad \left. + \frac{\partial^2 n_y}{\partial y^2} [-(n_y^2 n_z g_{1x}^*) + n_x n_y^2 g_{1z}^*] + \frac{\partial^2 n_x}{\partial y^2} (n_y^2 n_z g_{1y}^* - n_y^3 g_{1z}^*) \right) \\
& \quad + K_{22} \left( \frac{\partial n_x}{\partial y} (-2n_y n_z g_{1x}^* + 2n_x n_z g_{1y}^*) + \frac{\partial n_z}{\partial y} (-2n_x n_z g_{1y}^* + 2n_x n_y g_{1z}^*) \right. \\
& \quad \left. + \frac{\partial n_x}{\partial y} \frac{\partial n_z}{\partial y} (2n_x n_y g_{1x}^* - 2n_x^2 g_{1y}^* + 2n_z^2 g_{1y}^* - 2n_y n_z g_{1z}^*) \right. \\
& \quad \left. + \frac{\partial^2 n_z}{\partial y^2} (n_x^2 n_y g_{1x}^* - n_x^3 g_{1y}^* - n_x n_z^2 g_{1y}^* + n_x n_y n_z g_{1z}^*) \right. \\
& \quad \left. + \frac{\partial^2 n_x}{\partial y^2} [-(n_x n_y n_z g_{1x}^*) + n_x^2 n_z g_{1y}^* + n_z^3 g_{1y}^* - n_y n_z^2 g_{1z}^*] \right). \tag{A3}
\end{aligned}$$

4.  $g_2$ -torque balance

$$\begin{aligned}
& -\gamma_1 \left[ - \left( \frac{\partial n_x}{\partial t} (- \{ n_y [-(n_y g_{1x}^*) + n_x g_{1y}^*] \} + n_z (n_z g_{1x}^* - n_x g_{1z}^*) \right) \right. \\
& \quad \left. - \frac{\partial n_z}{\partial t} \{ -[n_x (n_z g_{1x}^* - n_x g_{1z}^*)] + n_y [-(n_z g_{1y}^*) + n_y g_{1z}^*] \} \right. \\
& \quad \left. - \frac{\partial n_y}{\partial t} \{ n_x [-(n_y g_{1x}^*) + n_x g_{1y}^*] - n_z [-(n_z g_{1y}^*) + n_y g_{1z}^*] \} \right. \\
& = K_{11} \frac{\partial^2 n_y}{\partial y^2} [-(n_x n_y g_{1x}^*) + n_x^2 g_{1y}^* + n_z^2 g_{1y}^* - n_y n_z g_{1z}^*] + \gamma_2 \left( n_x^2 n_y \frac{\partial v_x}{\partial y} g_{1x}^*/2 - n_y^3 \frac{\partial v_x}{\partial y} g_{1x}^*/2 - n_y n_z^2 \frac{\partial v_x}{\partial y} g_{1x}^*/2 \right. \\
& \quad \left. + n_x n_y n_z \frac{\partial v_z}{\partial y} g_{1x}^* - n_x^3 \frac{\partial v_x}{\partial y} g_{1y}^*/2 + n_x n_y^2 \frac{\partial v_x}{\partial y} g_{1y}^*/2 - n_x n_z^2 \frac{\partial v_x}{\partial y} g_{1y}^*/2 - n_x^2 n_z \frac{\partial v_z}{\partial y} g_{1y}^*/2 + n_y^2 n_z \frac{\partial v_z}{\partial y} g_{1y}^*/2 \right. \\
& \quad \left. - n_z^3 \frac{\partial v_z}{\partial y} g_{1y}^*/2 + n_x n_y n_z \frac{\partial v_x}{\partial y} g_{1z}^* - n_x^2 n_y \frac{\partial v_z}{\partial y} g_{1z}^*/2 - n_y^3 \frac{\partial v_z}{\partial y} g_{1z}^*/2 + n_y n_z^2 \frac{\partial v_z}{\partial y} g_{1z}^*/2 \right) \\
& \quad + \gamma_1 \left( n_x^2 n_y \frac{\partial v_x}{\partial y} g_{1x}^*/2 + n_y^3 \frac{\partial v_x}{\partial y} g_{1x}^*/2 + n_y n_z^2 \frac{\partial v_x}{\partial y} g_{1x}^*/2 - n_x^3 \frac{\partial v_x}{\partial y} g_{1y}^*/2 - n_x n_y^2 \frac{\partial v_x}{\partial y} g_{1y}^*/2 - n_x n_z^2 \frac{\partial v_x}{\partial y} g_{1y}^*/2 \right. \\
& \quad \left. - n_x^2 n_z \frac{\partial v_z}{\partial y} g_{1y}^*/2 - n_y^2 n_z \frac{\partial v_z}{\partial y} g_{1y}^*/2 - n_z^3 \frac{\partial v_z}{\partial y} g_{1y}^*/2 + n_x^2 n_y \frac{\partial v_z}{\partial y} g_{1z}^*/2 + n_y^3 \frac{\partial v_z}{\partial y} g_{1z}^*/2 + n_y n_z^2 \frac{\partial v_z}{\partial y} g_{1z}^*/2 \right) \\
& \quad + K_{33} \left( \frac{\partial n_y}{\partial y} \frac{\partial n_z}{\partial y} (-2n_x n_y n_z g_{1x}^* - 2n_y^2 n_z g_{1y}^* + 2n_x^2 n_y g_{1z}^* + 2n_y^3 g_{1z}^*) \right. \\
& \quad \left. + \frac{\partial^2 n_z}{\partial y^2} [-(n_x n_y^2 n_z g_{1x}^*) - n_y^3 n_z g_{1y}^* + n_x^2 n_y^2 g_{1z}^* + n_y^4 g_{1z}^*] \right)
\end{aligned}$$

$$\begin{aligned}
& + \frac{\partial n_x}{\partial y} \frac{\partial n_y}{\partial y} (2n_y^3 g_{1x}^* + 2n_y n_z^2 g_{1x}^* - 2n_x n_y^2 g_{1y}^* - 2n_x n_y n_z g_{1z}^*) \\
& + \frac{\partial n_y}{\partial y}^2 [-(n_x n_y^2 g_{1x}^*) + n_x^2 n_y g_{1y}^* + n_y n_z^2 g_{1y}^* - n_y^2 n_z g_{1z}^*] \\
& + \frac{\partial n_x}{\partial y^2} (n_x n_y^2 g_{1x}^* - n_x^2 n_y g_{1y}^* - n_y n_z^2 g_{1y}^* + n_y^2 n_z g_{1z}^*) \\
& + \frac{\partial n_z}{\partial y^2} (n_x n_y^2 g_{1x}^* - n_x^2 n_y g_{1y}^* - n_y n_z^2 g_{1y}^* + n_y^2 n_z g_{1z}^*) + \frac{\partial^2 n_x}{\partial y^2} (n_y^4 g_{1x}^* + n_y^2 n_z^2 g_{1x}^* - n_x n_y^3 g_{1y}^* - n_x n_y^2 n_z g_{1z}^*) \\
& + \frac{\partial^2 n_y}{\partial y^2} [-(n_x n_y^3 g_{1x}^*) + n_x^2 n_y^2 g_{1y}^* + n_y^2 n_z^2 g_{1y}^* - n_y^3 n_z g_{1z}^*] \\
& + K_{22} \left( \frac{\partial n_z}{\partial y^2} (-2n_x n_y^2 g_{1x}^* - 2n_x n_z^2 g_{1x}^* + 2n_x^2 n_y g_{1y}^* + 2n_x^2 n_z g_{1z}^*) \right. \\
& + \frac{\partial n_x}{\partial y}^2 (2n_x n_z^2 g_{1x}^* + 2n_y n_z^2 g_{1y}^* - 2n_x^2 n_z g_{1z}^* - 2n_y^2 n_z g_{1z}^*) + \frac{\partial n_x}{\partial y} \frac{\partial n_z}{\partial y} (-2n_x^2 n_z g_{1x}^* + 2n_y^2 n_z g_{1x}^* + 2n_z^3 g_{1x}^* \\
& - 4n_x n_y n_z g_{1y}^* + 2n_x^3 g_{1z}^* + 2n_x n_y^2 g_{1z}^* - 2n_x n_z^2 g_{1z}^*) \\
& + \frac{\partial^2 n_z}{\partial y^2} [-(n_x^3 n_z g_{1x}^*) - n_x n_y^2 n_z g_{1x}^* - n_x n_z^3 g_{1x}^* + n_x^4 g_{1z}^* + n_x^2 n_y^2 g_{1z}^* + n_x^2 n_z^2 g_{1z}^*] \\
& \left. + \frac{\partial^2 n_x}{\partial y^2} (n_x^2 n_z^2 g_{1x}^* + n_y^2 n_z^2 g_{1x}^* + n_z^4 g_{1x}^* - n_x^3 n_z g_{1z}^* - n_x n_y^2 n_z g_{1z}^* - n_x n_z^3 g_{1z}^*) \right). \tag{A4}
\end{aligned}$$

- 
- [1] M. Grmela, Phys. Rev. E **47**, 351 (1993).  
[2] P. G. de Gennes, *The Physics of Liquid Crystals* (Clarendon Press, Oxford, 1974).  
[3] R. B. Meyer, in *Polymer Liquid Crystals*, edited by A. Ciferri, W. R. Krigbaum, and R. B. Meyer (Academic Press, New York, 1982).  
[4] G. Kiss and R. S. Porter, Mol. Cryst. Liq. Cryst. **60**, 267 (1980).  
[5] N. J. Alderman and M. R. Mackley, Faraday Discuss. Chem. Soc. **79**, 149 (1985).  
[6] R. G. Larson and D. W. Mead, Liq. Cryst. **12**, 751 (1992).  
[7] R. G. Larson and D. W. Mead, Liq. Cryst. (to be published).  
[8] G. Srajer, S. Fraden, and R. B. Meyer, Phys. Rev. A **39**, 4828 (1989).  
[9] A. D. Rey, Macromolecules **24**, 4450 (1991).  
[10] R. G. Larson, J. Rheol. **37**, 175 (1993).  
[11] C. H. Gawhiller, Phys. Rev. Lett. **28**, 1554 (1972).  
[12] R. F. Bruinsma and C. R. Safinya, Phys. Rev. A **43**, 5377 (1991).  
[13] G. Marrucci, in *Elastic and Viscous Properties of Lyotropic Polymer Nematics*, edited by A. Ciferri (VCH, Weinheim, 1991).  
[14] T. Carlsson, Phys. Rev. A **34**, 3393 (1986).  
[15] Y. Farhoudi and A. D. Rey, J. Rheol. **37**, 289 (1993).  
[16] S. D. Lee and R. B. Meyer, in *Elastic and Viscous Properties of Lyotropic Polymer Nematics*, edited by A. Ciferri (VCH, Weinheim, 1991).  
[17] A. W. Chow, R. D. Hamlin, and C. M. Ylitalo, Macromolecules **25**, 7135 (1992).  
[18] K. Hongladarom and W. R. Burghardt, Macromolecules **26**, 785 (1993).  
[19] M. Srinivasarao, Ph.D. thesis, Carnegie Mellon University, Pittsburgh, 1990.  
[20] H. Yanase, Ph.D. thesis, Kyoto University, Kyoto, 1988.  
[21] M. Srinivasarao and G. C. Berry, J. Rheol. **35**, 379 (1991).  
[22] M. Srinivasarao, R. O. Garay, H. H. Winter, and R. S. Stein, in *Complex Fluids*, edited by E. Sirota, D. Weitz, T. Witten, and J. Israelachvili, MRS Symposia Proceedings No. 248 (Materials Research Society, Pittsburgh, 1991).  
[23] I. Zuniga and F. M. Leslie, Liq. Cryst. **5**, 725 (1989).  
[24] P. Pieranski and E. Guyon, Phys. Rev. Lett. **32**, 924 (1974); Commun. Phys. **1**, 45 (1976).  
[25] I. Zuniga, Phys. Rev. A **41**, 2050 (1990).  
[26] M. Luskin and T. Pan, J. Non-Newtonian Fluid Mech. **42**, 369 (1992).  
[27] W. H. Han and A. D. Rey, in *Complex Fluids* (Ref. [22]).  
[28] W. H. Han and A. D. Rey, J. Non-Newtonian Fluid Mech. **48**, 181 (1993).  
[29] W. H. Han and A. D. Rey, in *Theoretical and Applied Rheology*, Proceedings of the XIth International Congress on Rheology, edited by P. Moldenaers and R. Keunings (Elsevier, Amsterdam, 1992), p. 531; J. Non-Newtonian Fluid Mech. **50**, 1 (1993).  
[30] E. B. Becker, G. F. Carey, and J. T. Oden, *Finite Element Series Vols. I–VI* (Prentice-Hall, Englewood Cliffs, NJ, 1981).  
[31] R. Seydel, *From Equilibrium to Chaos: Practical Bifurcation and Stability Analysis* (Elsevier, Amsterdam, 1988).  
[32] Wolfram Research, Inc., computer code *Mathematica: A System for Doing Mathematics by Computer* (Wolfram Research Inc., Champaign, 1991); Stephen Wolfram, *Mathematica*, 2nd ed. (Addison-Wesley, Redwood City, CA, 1991).  
[33] G. Gaeta, Phys. Lett. **189**, 1 (1990).  
[34] J. D. Crawford, Rev. Mod. Phys. **63**, 991 (1991).  
[35] R. N. Thurston, Mol. Cryst. Liq. Cryst. **122**, 1 (1985).  
[36] J. L. Ericksen, Trans. Soc. Rheol. **13**, 9 (1969).  
[37] de Gennes, Phys. Lett. **41A**, 479 (1972).  
[38] P. Manneville, Mol. Cryst. Liq. Cryst. **70**, 223 (1981).



- [39] T. Carlsson, *Mol. Cryst. Liq. Cryst.* **104**, 307 (1984).
- [40] W. R. Burghardt and G. G. Fuller, *J. Rheol.* **34**, 959 (1990).
- [41] P. Pieranski, Ph.D. thesis, Universite Paris–Sud, Orsay, 1976.
- [42] K. Hiltrop and F. Fischer, *Z. Naturforsch. Teil A* **31**, 800 (1976).
- [43] A. D. Rey, *J. Rheol.* **34**, 425 (1990).
- [44] A. D. Rey, *J. Non-Newtonian Fluid Mech.* **40**, 177 (1991).
- [45] J. L. Ferguson, *Mol. Cryst. Liq. Cryst.* **1**, 293 (1966).
- [46] N. L. Kramarenko, I. V. Kurnosov, and Y. V. Naboikin, *Mol. Cryst. Liq. Cryst.* **47**, 7 (1978).
- [47] P. J. Collings, *Liquid Crystals: Nature's Delicate Phase of Matter* (Princeton University Press, Princeton, 1990).
- [48] S. Guido, N. Grizzuti, and G. Marrucci, *Liq. Cryst.* **7**, 279 (1990).
- [49] R. B. Bird, C. F. Curtiss, R. C. Armstrong, and O. Hassager, *Dynamics of Polymeric Liquids, Vol. 1* (Wiley, New York, 1987).
- [50] H. L. Doppert and S. J. Picken, *Mol. Cryst. Liq. Cryst.* **153**, 109 (1987).
- [51] J. Mewis and P. Moldenaers, *Mol. Cryst. Liq. Cryst.* **153**, 291 (1987).
- [52] N. Grizzuti, S. Cavella, and P. Cicarelli, *J. Rheol.* **34**, 1293 (1990).
- [53] S. M. Guskey and H. H. Winter, *J. Rheol.* **35**, 1191 (1991).
- [54] F. Cocchini, *J. Rheol.* **35**, 1171 (1991).
- [55] P. F. Erhardt, J. M. Pochan, and W. C. Richards, *J. Chem. Phys.* **57**, 5154 (1972).
- [56] J. M. Pochan and D. G. Marsh, *J. Chem. Phys.* **57**, 1193 (1972).
- [57] D. G. Marsh and J. M. Pochan, *J. Chem. Phys.* **58**, 2835 (1973).
- [58] H. A. Barnes, J. F. Hutton, and K. Walters, *An Introduction to Rheology* (Elsevier, Amsterdam, 1989).